Multi-omic analysis of SDHB-deficient pheochromocytomas and paragangliomas identifies metastasis and treatment-related molecular profiles

Richard Tothill

`rtothill@unimelb.edu.au`

University of Melbourne   https://orcid.org/0000-0003-4522-1184

Aidan Flynn

University of Melbourne

Andrew Pattison

Monash University

Shiva Balachander

Centre for Cancer Research and Department of Clinical Pathology, University of Melbourne

Emma Boehm

Centre for Cancer Research and Department of Clinical Pathology, University of Melbourne

Blake Bowen

Centre for Cancer Research and Department of Clinical Pathology, University of Melbourne

Trisha Dwight

Kolling Institute of Medical Research, Royal North Shore Hospital St Leonards

Fernando Rossello

Murdoch Children's Research Institute

Oliver Hofmann

Centre for Cancer Research and Department of Clinical Pathology, University of Melbourne

Luciano Martelotto

Adelaide University   https://orcid.org/0000-0002-9625-1183

Magnus Zethoven

Peter MacCallum Cancer Centre

Lawrence Kirschner

Division of Endocrinology, Diabetes and Metabolism, Department of Internal Medicine, The Ohio State University

Tobias Else

University of Michigan

Lauren Fishbein

Department of Medicine, Division of Endocrinology, Metabolism, Diabetes, University of Colorado

Anthony Gill

NSW Health Pathology, Department of Anatomical Pathology, Royal North Shore Hospital

Arthur Tischler

Tufts Medical Centre

Thomas Giordano

University of Michigan

Jane Noble

Children's Medical Research Institute

Tamara Prodanov

Eunice Kennedy Shriver National Institute of Child Health and Human Development

Roger Reddel

Children's Medical Research Institute   https://orcid.org/0000-0002-6302-6107

Alison Trainer

Peter MacCallum Cancer Centre

Hans Ghayee

University of Florida College of Medicine

Isabelle Bourdeau

Centre hospitalier de l'université de Montréal

Marianne Elston

Waikato Clinical Campus, University of Auckland

Nur Diana Binte Ishak

National Cancer Centre Singapore

Joanne Ngeow Yuen Yie

National Cancer Centre

Rodney Hicks

St Vincent's Dept of Medicine, University of Melbourne

Joakim Crona

Uppsala University   https://orcid.org/0000-0003-0677-4894

Tobias Åkerström

Uppsala University

Peter Stålberg

Uppsala University Hospital   https://orcid.org/0000-0002-9625-1394

Patricia Dahia

The University of Texas Health Science Center at San Antonio   https://orcid.org/0000-0002-7757-370X

Sean Grimmond

University of Melbourne Centre for Cancer Research   https://orcid.org/0000-0002-8102-7998

Roderick Clifton-Bligh

University of Sydney   https://orcid.org/0000-0002-1545-0368

Karel Pacak

National Institutes of Health   https://orcid.org/0000-0002-3541-3767

Article

Keywords:

Additional Declarations: There is **NO** Competing Interest.

1 **Title:** Multi-omic analysis of SDHB-deficient pheochromocytomas and paragangliomas identifies

2 metastasis and treatment-related molecular profiles

3

4 **Running Title**: Multi-omic analysis of SDHB pheochromocytomas

5

6 Aidan Flynn[1], Andrew D. Pattison[1], Shiva Balachander[1], Emma Boehm[1], Blake Bowen[1], Trisha Dwight[2],

7 Fernando Rosello[3], Oliver Hofmann[1], Luciano Martelotto[1], Maia Zethoven[3], Lawrence S. Kirschner[4],

8 Tobias Else[5], Lauren Fishbein[6], Anthony J Gill[7,8], Arthur S Tischler[9], Thomas Giordano[5], Tamara

9 Prodanov[10], Jane R Noble[11], Roger R Reddel[11], Alison H.Trainer [3,12], Hans Kumar Ghayee[13], Isabelle

10 Bourdeau[14], Marianne Elston[15], Diana Ishak[16], Joanne Ngeow Yuen Yie[16], Rodney J Hicks[17], Joakim

11 Crona[18a], Tobias Åkerström[18b], Peter Stålberg[18b], Patricia Dahia[19], Sean Grimmond[1], Roderick Clifton-

12 Bligh[†*2,7], Karel Pacak[†*10], Richard W Tothill[†*1,11]

13

14　　 1. Centre for Cancer Research and Department of Clinical Pathology, University of Melbourne, VIC,
15　　　　 Australia
16　　 2. Kolling Institute of Medical Research, Royal North Shore Hospital St Leonards NSW, Australia
17　　 3. Peter MacCallum Cancer Centre, Melbourne, Australia
18　　 4. Division of Endocrinology, Diabetes and Metabolism, Department of Internal Medicine, The Ohio
19　　　　 State University, Columbus, Ohio, USA.
20　　 5. University of Michigan, Ann Arbor, MI, USA
21　　 6. Department of Medicine, Division of Endocrinology, Metabolism, Diabetes, University of Colorado,
22　　　　 Aurora, CO, USA
23　　 7. Sydney Medical School, University of Sydney, Sydney NSW, Australia
24　　 8. NSW Health Pathology, Department of Anatomical Pathology, Royal North Shore Hospital, St
25　　　　 Leonards NSW, Australia
26　　 9. Tufts Medical Centre, Boston, MA, USA
27　　 10. *Eunice Kennedy Shriver* National Institute of Child Health and Human Development, Bethesda, MD,
28　　　　 USA
29　　 11. Children's Medical Research Institute, Faculty of Medicine and Health, The University of Sydney,
30　　　　 Westmead, Australia
31　　 12. Sir Peter MacCallum Department of Oncology, University of Melbourne, VIC, Australia
32　　 13. University of Florida and Malcom Randall VA Medical Center, Gainesville, FL, USA
33　　 14. Centre hospitalier de l'université de Montréal, Montreal, Canada
34　　 15. Waikato Clinical Campus, University of Auckland, Hamilton, New Zealand
35　　 16. National Cancer Centre, Singapore
36　　 17. St Vincent's Dept of Medicine, University of Melbourne, VIC, Australia
37　　 18. 18a Department of Medical Sciences, 18b Department of Surgical Sciences, Uppsala University,
38　　　　 Sweden
39　　 19. Div. Hematology and Medical Oncology, Department of Medicine, Mays Cancer Center, University
40　　　　 of Texas Health Science Center at San Antonio (UTHSCSA), TX, USA

41

42 † Contributed equally

43 *Corresponding authors

44 email: rtothill@unimelb.edu.au

45　　　 karel@mail.nih.gov

46　　　 roderick.cliftonbligh@sydney.edu.au

47

48

Abstract

Hereditary *SDHB*-mutant pheochromocytomas (PC) and paragangliomas (PG) are rare tumours with a high propensity to metastasize although their clinical behaviour is unpredictable. To characterize the genomic landscape of these tumours and identify metastasis biomarkers, we performed multi-omic analysis on 94 tumours from 79 patients using seven molecular methods. Sympathetic (chromaffin cell) and parasympathetic (non-chromaffin cell) PCPG had distinct molecular profiles reflecting their cell-of-origin and biochemical profile. *TERT* and *ATRX*-alterations were associated with metastatic PCPG and these tumours had an increased mutation load, and distinct transcriptional and telomeric features. Most PCPG had quiet genomes with some rare co-operative driver events observed, including *EPAS1*/HIF-2α mutations. Two mechanisms of acquired resistance to DNA alkylating chemotherapies were also detected - *MGMT* overexpression and mismatch repair-deficiency causing hypermutation. Our comprehensive multi-omic analysis of *SDHB*-mutant PCPG therefore identified features of metastatic disease and treatment response, expanding our understanding of these rare neuroendocrine tumours.

Main

Pheochromocytomas (PC) and paragangliomas (PG) are heritable neuroendocrine neoplasms arising from the sympathetic and parasympathetic nervous system. They are clinically remarkable for catecholamine hypersecretion (e.g. dopamine, noradrenaline, adrenaline) causing morbidity and occasionally death from cardiovascular sequelae[1,2]. PCPG are typically slow growing, but metastases develop in 10-20% of patients[3]. Current biomarkers are inadequate for predicting metastatic progression, which is currently incurable.

Metastatic risk, which guides surveillance recommendations[4-6], is highest in patients carrying constitutional pathogenic variants in *SDHB*. SDHB-deficiency and cellular succinate accumulation inhibits prolyl hydroxylase domain proteins (PHD1/2) leading to oxygen-independent stabilization of hypoxia inducible factor alpha (HIF-α) and HIF target gene activation - a phenomenon known as pseudohypoxia[7,8]. Succinate excess also inhibits other 2-oxoglutarate-dependent dioxygenases, including TET2 and jumonji histone lysine demethylases, causing genome-wide hypermethylation and epigenetic reprogramming[8,9]. While the causative role of SDHB-deficiency in metastatic PCPG is well founded, other genomic changes also likely contribute, such as *ATRX* and *TERT* mutations[10-16]. However, most PCPG genomic studies to date have used whole-exome sequencing, limiting detection of non-coding variants, structural alterations, telomeric features and DNA mutation patterns. Furthermore, these studies have predominantly analysed primary and non-metastatic tumours thereby limiting discovery of metastasis biomarkers.

Herein, we conducted an integrated multi-omic analysis of an internationally sourced and clinically well-annotated cohort of *SDHB*-mutant PCPG including parasympathetic head and neck PG (HN-PG) - a relatively understudied group to date. Importantly, paired primary and metastatic tumours were analysed in a subset of

85 cases. We found novel observations with respect to cell-of-origin, treatment response and clinical outcome
86 and confirmed telomeric dysfunction and other features in metastatic cases.

87

88 **Results**

89 **Whole genome and multi-omic analysis of *SDHB*-associated PCPG**

90 To characterize the genomic landscape of *SDHB*-mutant PCPG, we performed multi-omic analysis of an

91 international (A5 consortium) cohort representing 94 primary and/or metastatic PCPG tumours from 79

92 patients (Figure 1A)(*see* Supplementary Data 1 and 2 for clinical details). Analysis included whole-genome

93 sequencing (WGS) of tumour and matched blood (n=94), whole transcriptome sequencing (WTS) (n=91),

94 small-RNA seq (n=90), DNA methylation profiling (n=93) and C-circle analysis (n=89). Droplet-based (10x)

95 single nuclei (sn)RNA-seq and snATAC-seq was applied in a subset of cases (Figure 1B).

96

97 Review of histopathology and clinical data confirmed disease diagnosis in all cases. Paired

98 synchronous/metachronous primaries were analysed in four cases (E128, E136, E159, E229) and clonal

99 independence confirmed by discordant somatic profiles (Supplementary Figure 1). With respect to clinical

100 behaviour, 40 tumours from 37 patients were ostensibly non-metastatic with at least twelve-months of clinical

101 follow-up (median: 60 months, range 12 – 456). An additional eight primary PCPG from eight patients had

102 less than 12 months of clinical follow-up without metastases reported (termed *short clinical follow-up*). Thirty-

103 four of 79 patients had confirmed metastatic disease. Twenty-eight primary PCPG were analysed from 26

104 patients who developed metastases and in six patients at least one paired metastasis was available, confirming

105 the clonal link between the primary and metastatic tumours (termed *metastatic primary*) (Figure 1C). For 21

106 primary PCPG from 20 patients, metastasis was reported but metastatic tissue was not available (termed

107 *primary - metastasis reported*)(Figure 1C). Finally, in eight patients, one or more metastases were analysed

108 but a primary tumour was not analysed.

109

110 WGS confirmed pathogenic germline *SDHB*-mutations consisting of missense (n=41), nonsense (n=21),

111 frameshift insertions/deletions (n=6), large deletion events (n=7), and donor splice-site mutations (n=4)

112 (Figure 1D). Two recurrent large deletion events were identified in two or more unrelated patients

113 (chr1:g.17052136-17054668_del,   chr1:g.17048756-17064432_del).   WGS   showed   variable   length

114 homologous DNA sequence at the breakpoint ends of a subset of the large deletions, implicating homologous

115 recombination as a potential cause of the germline deletions (Supplementary Figure 2). Somatic loss-of-

116 heterozygosity (LOH) at 1p36.13 with or without somatic copy-loss was detected in all tumours and SDHB

117 immunohistochemistry confirmed tumoural SDH-deficiency.

118

119 **Molecular profiling confirms genotype-subtype and cell-of-origin transcriptional profile**

120 Molecular subtyping is known to reflect the genotypic features of PCPG[13,17-21]. To confirm genotype-

121 phenotype relationships among A5 tumours we applied UMAP clustering to WTS (n=91), small-RNA-seq

and DNA methylation datasets. Published RNA-seq data across a spectrum of PCPG genotypes was included for comparison[13,14,20]. Here, we used the C1/C2 annotation based on seven PCPG gene-expression subtypes previously defined by single-nuclei and bulk gene-expression analysis[22]. As expected, all A5 *SDHB*-mutant tumours clustered among C1A (SDHx) tumours by WTS. UMAP of the small-RNA-seq data showed a similar clustering pattern; however, four A5 tumours from two patients clustered with an outlier group consisting of unrelated genotypes (Figure 2B). This small-RNA-seq outlier group included C2Bi (*MAX*) PCPG that frequently exhibit loss-of-heterozygosity of chr14q and silencing of the imprinted *DLK1-MEG3* miRNA cluster located on chr14q31-32[20] (Supplementary Figure 3). By DNA methylation profiling, *SDHB*-mutant PCPG independently of other PCPG genotypes with the exception of one tumour (E229-P1) (Figure 2C), and *SDHB*-mutant tumours showed genome-wide hypermethylation (Supplementary Figure 4), consistent with a prior report[9]. Unsupervised clustering therefore confirmed the expected molecular profile of the A5 *SDHB*-mutant tumours as well as the pathogenicity of constitutional *SDHB* variants.

UMAP clustering of only the A5 tumours showed clear separation of parasympathetic (non-chromaffin cell) HN-PG from sympathetic (chromaffin cell) PCPG (Figure 2D-F). Two mediastinal dopamine-secreting PG (E148-P1, E155-P1) clustered with the HN-PG group, suggesting these tumours may be non-chromaffin cell paragangliomas[23] while one HN-PG (E185-P1) and one AT-PG (E128-P2) showed variable clustering. Supervised differential expression analysis between HN-PG and sympathetic PCPG identified 4615 genes and 36 microRNAs (adjusted p-value < 0.05, log fold change > 1) (Supplementary Data 3 and 4). HN-PG and the suspected non-chromaffin mediastinal tumours had low expression of the chromaffin cell marker *CARTP*[24], neural transcriptional regulators (*TFAP2B, TOX3, GATA3, POU4F, NEUROG2, PAX2), HOX* genes (*HOXA1-10, HOXB4, HOXB6-9, HOXC4-HOXC13*), and the long non-coding RNA *HOTAIR* (Figure 2H, Supplementary Figure 5). Similar to the *HOX* gene clusters, clustered genes on chr12q24.32 including *TMEM132C* and lncRNAs were also lowly expressed. Concordant DNA methylation patterns were also observed (Figure 2G, Figure 2I, Supplementary Figure 6).

HN-PG are predominantly biochemically silent and accordingly catecholamine biosynthesis genes including *TH* and *DBH* were lowly expressed (Figure 2J). Although most sympathetic PCPG are biochemically active, a small number of A5 cases had normal catecholamine levels and such tumours also had low *TH* expression. Some patients with HN-PG/non-chromaffin cell tumours and sympathetic PCPG had elevated plasma 3-methoxytyramine (3-MT) (a dopamine metabolite[25,26]) and these tumours had low *DBH* expression - DBH being necessary to convert dopamine to norepinephrine. Low *TH* and *DBH* expression corresponded with gene-promoter methylation (Supplementary Figure 7). Meanwhile, variable expression of the norepinephrine transporter (*SLC6A2*) was observed with gene-promoter methylation corresponding with low expression in sympathetic PCPG (Supplementary Figure 8). Low *SLC6A2* (NET) expression is clinically relevant since NET is required for uptake of theranostic agents e.g.[123/124/131]I-meta-iodobenzylguanidine (MIBG)[27,28].

With respect to neurotransmitters, *TPH1* (tryptophan hydroxylase), essential for serotonin (5-HT) synthesis, was overexpressed in the HN-PG/non-chromaffin cell tumours (Figure 2G, Supplementary Figure 9). TPH is known to be expressed in glomus cells of the carotid body (presumed the HN-PG cell-of-origin)[29], and 5-HT storage vesicles have been observed in some HN-PG, although urinary 5-HIAA is not elevated in most HN-PG patients[30]. Meanwhile, while immunohistochemical detection of choline acetyltransferase (*CHAT*) has been reported in HN-PG[31], *CHAT* mRNA was not overexpressed in these tumours (Supplementary Figure 10).

Genome-wide mutational features of *SDHB*-deficient PCPG

Consistent with prior studies, therapy naive PCPG (n=84) had a low mutation burden (median =0.32, range 0.03-4.24 mut/Mb)[11,13,14,20]. Single-base substitution (SBS) signature analysis (COSMICv3) showed predominantly age-related or clock-like mutational signatures (SBS1, SBS5) (Figure 3A). With respect to doublet base substitutions (DBS) the predominant patterns were DBS 2, 4, 9 and insertion/deletion (ID) signatures ID 5, 8 and 9. With respect to systemic cytotoxic treatments, 10/94 (12%) of tumours were resected post-treatment (Supplementary Figure 11) and chemotherapy-related mutational signatures were observed in some cases including SBS11 (DNA alkylation) (discussed below).

PCPG tumours showed recurrent patterns of chromosomal changes similar to observations in previous studies[13,14,18] including loss of chr1p, chr2q, chr3, chr8p, chr11, chr17p and chr22 (GISTIC q<0.05) (Figure 3B, Supplementary Figure 12). Significant copy-number gains were observed on chr1q in sympathetic (chromaffin cell) PCPG, while parasympathetic (HN-PG/non-chromaffin cell) tumours had frequent loss of chr1q. A minority of tumours had chromothripsis (n=6) or genome-doubling (n=9), as previously reported in PCPG[13,14]. Notably, we identified significant chr7 gains in the metastatic group (GISTIC q<0.05).

Few genes were recurrently altered and only 15 cancer-related genes had >1 predicted pathogenic mutation using Cancer Genome Interpreter[32] (Figure 3C, Supplementary Data 5). Consistent with prior studies, *TERT* and *ATRX* were the most frequently mutated genes[11,13,15] (discussed in detail below). *ATRX* mutations were significant drivers using the dN/dS[33] method while *TERT* promoter *(pTERT)* mutations were significant using OncoDriveFML[34]. Two tumours had somatic *EPAS1* (HIF-2α) pathogenic variants near codon 531 (prolyl) targeted by PHD2 (Figure 3D). One *EPAS1* mutation (E230-P1, NP_001421.2:p.Tyr532Cys) was previously described in a PCPG patient with polycythemia[35,36], while a second *EPAS1* mutation (E183-P1, NP_001421.2:p.Asp539Gly) involved the same codon as a previously reported *EPAS1* pathogenic variant[37]. Other recurrently mutated cancer genes included chromatin modifiers *KMT2C (n=2)* and *BCOR (n=2)*. *TP53* somatic mutations were found in three metastatic tumours consistent with a known low frequency in PCPG[13,14,20]. Finally, a *MYCN* hotspot mutation was found in one tumour (E129-P1, NP_005369.2:p.Pro44Leu), as previously reported in another study[38].

Somatic *TERT* mutations, structural rearrangement and promoter methylation

Hotspot p*TERT* mutations (chr5:1295113G>A, chr5:1295135G>A, GRCh38) were identified in 14 metastatic cases (17.7%). Targeted deep sequencing of p*TERT* excluded potential sub-clonal mutations in the other cases. snATAC-seq data showed a promoter peak central to the *de novo* ETS binding site[39] in three p*TERT* mutants tested and all snATAC-seq reads had the somatic variant, confirming open chromatin (Figure 4A). Chromothripsis of chromosome 5 created an *AFF4-TERT* fusion in one case (E123) (Figure 4B). WGS supported a DNA breakpoint in *AFF4* 3-prime of untranslated exon 1 and DNA sequence 390 bp upstream of the *TERT* transcription start site (Figure 4Bii). RNA-seq split-reads supported a fusion transcript involving *AFF4* exon 1 spliced to *TERT* exon 3 (Figure 4Biii). This validates our prior report of *TERT* structural rearrangements in PCPG[16] but to our knowledge is the first *TERT*-fusion reported in PCPG.

All *TERT*-altered cases had elevated *TERT* expression with the highest expression observed in the *AFF4:TERT* fusion tumour. *TERT* copy-number gain did not correlate with *TERT* overexpression in the absence of *TERT* mutation or fusion events (Figure 4C). We found *TERT* promoter hypermethylation including the THOR domain (probes cg11625005, cg10767223) in *TER*T-altered PCPG, as previously described[15] (Figure 4D). *TERT* promoter hypermethylation and concordant overexpression was also observed in a single metastatic *TERT* wild type tumour (E171-M1) (Figure 4D).

ance* *ATRX* alterations are associated with the ALT phenotype

Pathogenic *ATRX* mutations included nonsense and splice-site mutations, small frameshift insertions or deletions, and a large deletion in one case (Figure 5A). One missense *ATRX* mutation (unknown significance) was detected (NM_000489.6:c.6778C>T, NP_000480.3:p.H2260Y). *ATRX* expression was low in most *ATRX* altered cases, presumably due to nonsense-mediated decay (Supplementary Figure 13).

Alternative lengthening of telomeres (ALT) is a known feature of *ATRX*-altered PCPG and other cancer types[12]. C-circle analysis was done to predict ALT activity[40] and C-circles were detected in all *ATRX*-altered and one *TERT*-altered primary tumour (E143-P1) (discussed below)(Figure 5B). As expected, the telomeric tumour:blood ratio, a proxy for tumour telomere length, was higher in *ATRX*-altered compared to *TERT*-altered or *TERT*/*ATRX* wild type tumours (Student's t-test p-value < 0.00025) with no significant difference in telomeric DNA content observed between the latter two groups. Long telomeres in the absence of C-circles were detected in four *ATRX*/*TERT* wild type PCPG, including two HN-PG.

ALT features can include aberrant telomeric variant repeat (TVR) usage, intrachromosomal insertion of telomeric DNA and expression of telomeric repeat-containing RNA (*TERRA*)[41]. Relative TVR usage was altered in C-circle positive *versus* negative tumours (Figure 5C). Normalized to total read count only three TVRs (TTAGGG, GTTGGG, GTAGGG) remained significant after false-discovery rate correction (Benjamini & Hochberg, p<0.1). When normalized to the telomeric reads the canonical TVR (TTAGGG) was

proportionally more abundant in C-circle positive compared to negative tumours. Only one intrachromosomal telomeric insertion was detected in an *ATRX* altered case (data not shown), while *TERRA* expression was elevated in *ATRX* altered tumours, although was not statistically significant (Two-sided Student's t-test p>0.05)(Figure 5D).

TERT/ATRX alterations are associated with metastatic progression and late somatic events

TERT/ATRX alterations were found in 21/34 (61%) metastatic cases and significantly associated with metastasis (Pearson's Chi-squared p-value 9.349e-08). Only one non-metastatic tumour (E156-P1) had a p*TERT* mutation; however, this case had a short clinical follow-up (Figure 6A). Evidence for late development of p*TERT* mutations was found in two cases: 1) E146 where the primary was *TERT* wild type but the paired metastasis was p*TERT* mutant and 2) case E143 where a subclonal p*TERT* mutation was detected in the primary (VAF = 10.3%) but higher VAF was detected in two paired metastases (E143-M1 VAF=33%, E143-M2 VAF= 28%), indicating all metastatic cells were p*TERT* mutant (Figure 6B). Interestingly, the subclonal p*TERT* mutant primary (E143) also had detectable C-circles and longer telomeres, but these ALT features were absent in both metastases. The data therefore suggests the *pTERT* mutation and ALT features had co-existed but were likely within different cell subpopulations, while only the p*TERT* mutant cells metastasized.

Ten primary tumours from patients with metastatic disease did not have *TERT/ATRX*-alterations, but the late acquisition of *TERT/ATRX* alterations and presence in metastatic cells could not be excluded given that the metastatic tissue was not sequenced. However, metastasis in the absence of *TERT/ATRX* alterations was also evident in three metastatic tumours for two patients (E158, E159). These metastases had no other evidence of a TLM (i.e., they did not overexpress *TERT*, and had neither detectable C-circles nor an increased telomere length ratio) and had no recurrent cancer gene alterations that may explain metastatic progression. Interestingly, we found the tumour mutation burden was significantly elevated in *TERT/ATRX*-altered PCPG (One-tailed Student's t-test p<0.001) consistent with a previous study[11], but metastases from the *TERT/ATRX* wild type cases had a low mutation burden (Figure 6C). Interestingly, while it is also known that a larger primary tumour is associated with metastatic risk, only patients with *TERT*-altered tumours had larger primaries when contrasting to patients without *TERT/ATRX* alterations (Two-sided students t-test, p<0.05)(Figure 6D). Finally, survival analysis showed a significant association with poorer outcome in the *TERT/ATRX*-altered group (Supplementary Table 1, Supplementary Figure 14).

Transcriptional patterns in TERT/ATRX-altered and metastatic PCPG

We next assessed transcriptional changes in *TERT* and *ATRX*-altered PCPG, respectively, by contrasting each group independently to non-metastatic PCPG and directly to each other. Furthermore, we contrasted all metastatic and non-metastatic PCPG in a separate analysis (Figure 7A). All HN-PG/non-chromaffin tumours (defined by transcriptional profile) were excluded given the absence of *TERT/ATRX* alterations in these tumours. Furthermore, we excluded low tumour purity cases (<50% estimated by WGS data) and a subclonal

TERT-mutant case. Contrasting the *TERT* and *ATRX*-altered tumours to non-metastatic tumours we found 1,152 and 1,448 differentially expressed genes, respectively (Supplementary Data 6). Some of these genes were common to both analyses (n=273), as well as when contrasting all metastatic and non-metastatic tumours (n=180).

Consistent with prior studies, genes overexpressed in metastatic PCPG were enriched for cell cycle and proliferation gene ontologies[11,22]. *MKI67* was among the top overexpressed genes in keeping with elevated Ki67 IHC staining (Figure 7B). Other genes included cell cycle regulators (e.g. *TOP2A*, *BUB1*, *FOXM1*, *AURK2B*, *CDK1*), that were highly correlated with *MKI67* expression (r>0.88). Other genes overexpressed in metastatic PCPG included the polycomb repressor complex 2 gene *EZH2*, as previously described[22], and the transcription factors *OTX1* and *TPX1*.

Long non-coding RNAs and pseudogenes were enriched in genes differentially expressed in *ATRX*-altered tumours (Pearson's Chi-squared p-value=9.9e-14)(Supplementary Figure 15). The serine/threonine protein kinase *RIPK4* was also overexpressed, while genes downregulated in *ATRX* altered tumours included the p53-dependent G2M cell cycle regulator *RPRM* and the GTP-binding gene *DRG2* – the latter gene also implicated in G2M cell cycle checkpoint control (Figure 7C)[42]. Other genes down-regulated in *ATRX*-altered tumours included *USE1*, *SULT4A1* and the nuclear-encoded mitochondrial gene *COX17*. Many differentially expressed genes were also within differentially DNA methylated regions (Figure 7C). Gene-expression in neoplastic cells was confirmed using the snRNA-seq data and differential expression in *ATRX* mutant tumours was validated using independent bulk RNA-seq datasets[13,14] (Figure 7D). Meanwhile, few genes were uniquely expressed in *TERT*-altered tumours but included *IRX3*, *SDK1* and *TRIP13* (Figure 7E).

Treatment-related mutagenesis and resistance to DNA alkylating chemotherapy

DNA alkylating chemotherapies (e.g. dacarbazine and temozolomide) are common treatments for metastatic PCPG[43]. Two patients had paired tumours taken before and after cyclophosphamide, vincristine and dacarbazine (CVD) treatment. Case E169 had a para-aortic AT-PGL with distant lung, liver, and bone metastases (Figure 8A). Tumours resected before (lung, E169-M1) and after (spinal disease, E169-M2) 23 cycles of CVD were used for genomic analysis. Paired E169 tumours had a high number of shared SNVs (n=3158) including mutations in *TERT* and *BCOR;* however, the number of SNVs doubled in the post-CVD (n=12702) tumour including mutations in *TP53*, *RPL5* and *POLE* (DNA Polymerase Epsilon) (Figure 8B). SBS signatures also changed in the post-treatment sample with increased representation of SBS8, SBS12, SBS16 and SBS21 as well as indel signature ID1 (Figure 8C). However, elevated SBS11 associated with DNA alkylating chemotherapy and SBS14 associated with DNA polymerase epsilon-deficiency was absent. Importantly, *MGMT* was overexpressed in the post-treatment tumour (E169-M2) (Figure 8D). *MGMT* overexpression is a known temozolomide resistance mechanism in glioblastoma cells[44] and therefore potentially an acquired dacarbazine resistance mechanism in PCPG.

A second case (E167) had a left adrenal primary PC and then 14 years later developed HN-PGL and metastatic disease in the hip (Figure 8E). The patient progressed with development of liver metastases after ^{131}I-MIBG therapy and was subsequently treated with 22 cycles of CVD. Further progression occurred with new intracranial and osseous disease. Liver and intracranial metastases represented disease pre- and post-CVD treatment respectively, with clonal relatedness confirmed by common SNVs (n=2407) including a p*TERT* mutation (Figure 8F). *MGMT* expression was low in both tumours (Figure 8D). The post-CVD metastasis acquired more than a million additional SNVs corresponding to a strong SBS11 signature. Interestingly, the post-treatment intracranial metastasis (E167-M2) had a somatic *NRAS* (NP_002515.1:p.G12A) mutation and predicted to have elevated MAP kinase pathway activity by WTS (Supplementary Figure 16). Importantly, a protein truncating *MLH1* splice-site mutation (chr3:g.37091976G>A) was detected in the post-CVD metastasis with concordant loss-of-heterozygosity and low *MLH1* expression (Figure 8F). Canonical SBS mismatch-repair (MMR) mutational signatures (e.g. SBS6, SBS14, SBS21) were not detected in the post-CVD treated tumour; however, insertion/deletion signature ID2 was elevated and insertion/deletion events at microsatellite sites revealed a high MSI-score (11.7 microsatellite indels per mega base) in the post-CVD tumour (E167-M2), which is above the prescribed microsatellite instability threshold (>4)(Supplementary Figure 17).

Pathogenic variants in MMR genes (*MLH1*, *MSH2*, *MSH6, PMS2*) as well as treatment-related hypermutation and SBS11 have been described in temozolomide-treated glioblastomas[45,46] and more recently also pancreatic neuroendocrine tumours[47]. To search for evidence of MMR-deficiency in additional PCPG we analysed variant data from AACR Project GENIE (release 13), representing comprehensive cancer panel data for 75 PCPG. We identified one hypermutated case with a dominant C>T mutational pattern and an *MSH6* variant predicted to be a driver by Cancer Genome Interpreter (GENIE-DFCI-001077-11300, NP_000170.1:p.G162E) (Figure 8I-J). Furthermore, we performed 523-gene panel sequencing of plasma cell-free (cf) DNA from a patient with *SDHB*-associated PCPG with high disease volume as shown by ^{18}F-FDG-PET (Figure 8K). Blood was taken after three cycles of temozolomide combined with [177]Lutetium-DOTA-octreotate. The patient had high fraction of circulating tumour (ct) DNA (45%) (Figure 8L). Hypermutation was evident in cfDNA with a predominance of C>T transitions corresponding to SBS11 (Figure 8J), although most C>T mutations had low VAF (~0.5%) in contrast to truncal mutations involving p*TERT, MYCN, NUTM1* and *MAP2K1* (VAF>10%) (Figure 8M). A mutation in an MMR gene was not detected; however, the hypermutated clone likely represented a small fraction of total disease volume therefore detection of an MMR gene mutation may have fallen below the detection limit of the cfDNA assay (VAF>0.5%).

Discussion

We performed a comprehensive genomic analysis of *SDHB*-associated PCPG thereby creating a data resource to understand development of metastatic disease in these patients. Consistent with prior studies, most PCPG had stable genomes with few recurrently mutated cancer genes[11,13,14,20]. Importantly, we confirm *SDHB*-mutant PCPG are molecularly distinguishable from other PCPG genotypes, while parasympathetic (non-chromaffin) tumours including HN-PG had a very distinct molecular profile. Our data confirms *TERT* and *ATRX* alterations are the most common secondary driver events in PCPG and are enriched in metastatic disease[11,13,15]. However, a small number of metastatic PCPG lack *TERT/ATRX* alterations, suggesting yet unidentified mechanisms of metastatic progression in these cases.

Mutual exclusivity of *TERT/ATRX*-alterations in PCPG suggests these events have a common and potentially redundant role in metastasis. Both genes are involved in telomere maintenance - a hallmark of cancer[48]. However, given the majority of PCPG, including a subset of metastatic PCPG, have no obvious telomere lengthening mechanism (TLM), how, or indeed whether, these tumours maintain their telomeres is unknown. While methods such as the Telomere Repeat Amplification Protocol (TRAP)[49] and the C-circle assay are required to exclude the presence of a known TLM in tumour cells, absence of TLM has also been reported in other neuroepithelial cancers[50,51]. Meanwhile, while *ATRX/TERT* alterations were strongly associated with metastatic progression, the presence of long telomeres in the absence of TLM appears unlikely to be sufficient to drive metastatic progression[15].

ATRX is a SWI-SNF chromatin remodelling protein with multiple functions beyond telomeric regulation, while TERT is also thought to have non-canonical functions[52]. We observed that increased cell cycle activity appears to be common to *ATRX/TERT* altered PCPG, which is consistent with prior studies[11,22] and in keeping with increased Ki67 staining within metastatic PCPG[53]. Experimental models implicate *ATRX* and *TERT* in regulating cell cycle activity. For instance, ATRX binds to regulatory elements of cell cycle genes including *CHEK1,* as previously reported in a glioblastoma model[54]. Intriguingly, we found repression of *RPRM* and *DRG2* in *ATRX* altered PCPG, which are known to regulate the G2M cell cycle checkpoint[42,55]. It remains to be determined if *RPRM* and *DRG2* are ATRX target genes. TERT can also promote cellular proliferation and has a pro-survival function. For instance, cellular proliferation can be inhibited by wild-type reversion of a p*TERT* mutation in a glioblastoma cell line[56]. Furthermore, catalytically inactive TERT can rescue TERT-null cells, indicating a pro-survival function that is independent of telomerase activity[57]. How TERT promotes cellular proliferation is poorly understood and may be cell type and context dependent. Prior studies have shown TERT occupancy at gene-promoters including tRNAs[58] while TERT has also been shown to interact with oncogenic pathways involving MYC, WNT/B-catenin or NFkB[52]. Given few differentially expressed genes were restricted to *TERT*-altered PCPG, experimental models will be required to understand any non-canonical TERT functions in PCPG.

ATRX/TERT alterations have potential implications for treatment and surveillance. An increased sensitivity of *ATRX*-altered tumour cells to DNA damage response (DDR) inhibitors targeting ATM[54], WEE1[59], ATR and PARP[60,61] has been reported in other neuroectodermal cancers, and therefore might be effective in PCPG. Sensitivity to radiosensitizing DDR-targeting drugs in combination with radionuclide therapies (e.g. [177]Lutetium-DOTA-octreotate or ^{131}I-MIBG) also warrants investigation in the context of *ATRX/TERT* alterations[62,63]. Although we confirmed *TERT/ATRX*-alterations are associated with metastatic disease, the utility of these mutations as predictive biomarkers may be limited by the late timing of these events. Detection of *TERT/ATRX* alterations by cfDNA analysis may be a viable alternative to tissue biopsies, although the broader utility of cfDNA detection in PCPG still requires further validation.

DNA alkylating agents are commonly used for PCPG but there are currently no validated biomarkers to predict treatment response. We identified hypermutation together with MMR mutations (e.g. *MLH1*, *MSH6)* or *MGMT* overexpression in dacarbazine or temozolomide-treated PCPG. These observations are potentially clinically important. Firstly, monitoring PCPG patients for development of MMR mutations, SBS11 or potentially *MGMT* overexpression may indicate development of treatment-resistant cells. Secondly, MMR-mutations may sensitize tumour cells to other treatments. For instance, hypermutation can theoretically generate neoantigens causing T-cell recognition in tumours, making them more immunogenic and potentially more sensitive to immune checkpoint inhibition (ICI), although this theory is tempered by observations in glioblastoma where temozolomide-induced hypermutation did not translate to ICI-response[46]. Synthetic lethality could be another approach in MMR-deficient tumours, including use of WRN helicase inhibitors[64]. Further investigation is required to determine whether these treatments are efficacious in MMR-deficient PCPG.

Although therapeutically actionable mutations are rare in *SDHB*-mutant PCPG, co-operative drivers can still represent potential treatment opportunities in some patients. In particular, somatic *EPAS1* variants in *SDHB*-mutant tumours may have translational relevance. It is currently unknown whether HIF2α inhibitors (e.g. belzutifan) are effective for *SDHB*-mutant PCPG, but it is plausible that co-operative *EPAS1* mutations could make these tumours more sensitive[65]. Screening for co-operative somatic *EPAS1* mutations in *SDHB*-mutation carriers should therefore be employed for future HIF2α inhibitor clinical trials. Although we have reported the most comprehensive analysis of *SDHB*-mutant PCPG to date, future studies will be needed to validate our findings and identify additional low frequency genomic features that may be used as clinical biomarkers and future treatment targets.

Competing interests

The authors declare no competing interests.

Author Contribution

RWT, KP and RCB conceived the study. AF, ADP, SB, EB, BB, TD, FR, LM, MZ and JRN performed experiments and data analysis. AST and AJG performed pathology review and analysis. LSK, TE, DI, LF, AJG, OH, AST, TG, RRR, HKG, AHT, IB, MSE, JNYY, RJH, JC, TA, PS, PD, RCB and KP provided material support recruited patients or curated clinical data. AF, RCB, KP and RWT, wrote the manuscript. All authors edited and approved the final manuscript.

Methods

Patient samples and human research ethics

The research was conducted under and approved protocol of the human research ethics committee at Peter MacCallum Cancer Centre under the guidelines of the National Health and Medical Research Council and in accordance with the Helsinki Declaration of 1975, as revised in 1983. Patients were recruited at 11 sites under protocols approved by their respective institutional review boards with written informed consent without any compensation. Patient recruitment sites included those forming the American-Australian-Asian-Adrenal-Alliance (A5) International Research Consortium including the Peter MacCallum Cancer Centre (Australia), the Kolling Institute Neuroendocrine Tumour Bank under a protocol approved at North Sydney Local Health District (Australia), National Institute of Health (USA), University of Colorado (USA), University of Texas Health Science Center at San Antonio (USA), University of Florida (USA), University of Michigan (USA), Centre hospitalier de l'université de Montréal (Canada), as well as four non-A5 sites at Tufts Medical Centre

448 (USA), Waikato Hospital (New Zealand), the National Cancer Centre (Singapore), and Uppsala University
449 (Sweden)

450

451 **Tissue sample review and nucleic acid extraction**
452 Tissue samples were assessed for tumour cell content by a single pathologist (AG) by haematoxylin and
453 eosin staining of 4uM cryosections. Ten serial 10uM sections were taken for nucleic acid extraction adjacent
454 to the H&E reviewed sections. If required, microdissection of tissue was performed on ethanol fixed and
455 stained fresh tissue sections to dissect tumour regions from the sectioned material. DNA was extracted from
456 tissue samples and matched patient whole blood using the DNeasy® Blood & Tissue kit (Qiagen, Germany)
457 according to manufacturer's protocol. Total RNA was extracted from tissue using the miRNeasy mini kit
458 (Qiagen, Germany) according to the manufacturer's protocol. Nucleic acids were quality control checked by
459 Agilent TapeStation microfluidic electrophoresis (Agilent, USA) and NanoDrop spectrophotometer (Thermo
460 Fisher Scientific, USA).

461

462 **Targeted Amplicon Sequencing**
463 To validate mutations of interest, targeted amplicon sequencing was done using custom primers compatible
464 with universal indexed primers for Illumina cluster generation. PCR amplification for the region of interest
465 was done in a single well (for each patient sample) and the expected PCR amplicon product then verified by
466 agarose gel electrophoresis. Multiple amplicons for each patient sample were pooled, purified, and then
467 barcoded with the index primers, quantified by fluorometer (Qubit dsDNA High-sensitivity, USA) and then
468 sequenced on a MiSeq using a V3 300 cycle kit (Illumina, USA). FASTQ files were aligned to human genome
469 (GRCh38) using BWA-MEM and BAM files were visualized in IGV[66] to confirm variant of interest and
470 record the variant allele frequency.

471

472 **Whole genome sequencing**

473

474 **Library preparation**
475 Libraries were prepared using the Illumina® TruSeq™ DNA Nano library preparation method according to
476 the manufacturer's instructions at The University of Melbourne Centre for Cancer Research (UMCCR)
477 using 200ng input DNA and a 550 base pair insert size. Samples were sequenced in separate batches on the
478 Illumina® Nova-Seq 6000 according to manufacturer's instructions (Illumina, USA).

479

480 **WGS alignment and small variant calling**
481 BCL files were demultiplexed and converted to FASTQ files with Illumina® *bcl2fastq* (version 2.20.0.422)
482 with default settings (including adapter trimming). Alignment and variant calling steps were run using the
483 *bcbio-nextgen* cancer somatic variant calling pipeline (version 1.2.4-76d5c4ba)
484 (https://github.com/bcbio/bcbio-nextgen). The versions of all programs used by *bcbio-nextgen* are

485 additionally shown in Supplementary Table 2. Briefly, the tumour and normal sequencing data in FASTQ

486 format were first processed by *Atropos* (version 1.1.28)[67] to clip homopolymers (minimum 8 bases) from the

487 ends of reads. Trimmed FASTQ files were aligned to the human genome (GRCh38) with *BWA-mem*

488 (version 0.7.17)[68] with predominantly default settings. The two exceptions were that the -*M* flag was enabled

489 to mark shorter split read hits as a secondary alignment and seeds with > 250 occurrences were skipped

490 (reduced from the default 500).

491

492 Germline variants were called by *vardict* (version 1.8.2)[69], GATK *HaplotypeCaller* (GATK version

493 4.1.8.1)[70,71] and *Strelka2* (version 2.9.10)[72] callers. Somatic variants were called by *vardict*, *Mutect2* (see

494 GATK version)[73] and *Strelka2* (version 2.9.10) variant callers. In both instances a variant was accepted as

495 true if it was detected by 2 of the 3 callers. Somatic variants were further post-processed by *umccrise*

496 (version 1.2.0-rc.1, https://github.com/umccr/umccrise). To further reduce spurious variant calls, a variant

497 blacklist was generated by counting supporting reads for all detected somatic variants across all normal

498 BAM files using SAMtools[74] (version 1.12) *mpileup*. Any somatic variants that were supported by three or

499 more reads in more than two normal controls were excluded.

500

WGS copy number and structural variant calling

502 Structural variants (SV) were called with *GRIDSS* (version 2.8.0)[75]. *GRIDSS* output was annotated for repeat

503 sequences using *RepeatMasker* (version 4.1.5) and filtered for somatic SVs using *GRIPPS* (version 1.11).

504 To ensure high quality somatic calls, all SVs passing *GRIPSS* filtering were examined in the raw output of

505 *GRIDSS* across all samples. Any SV (based on exact genomic coordinates) that was observed (whether

506 ultimately rejected or passed) in more than two unrelated samples was removed. Finally, SVs were required

507 to have either a minimum of three supporting split reads or paired reads, or a combination of at least one

508 split and one paired read. Somatic copy number profiles were generated using *PURPLE* (version 3.1,

509 https://github.com/hartwigmedical/hmftools) from input generated by *COBALT* (version 1.11), *AMBER*

510 (version 3.5), and *GRIDSS*. Structural variants were further annotated with *Linx* (version 1.16) using the

511 output from *PURPLE*.

512

Telomere length estimation and telomere variant repeat detection

514 Telomere content was estimated from WGS for each tumour and normal pair using *TelomereHunter* (version

515 1.1.0)[76] with default parameters. Telomere content was computed from the number of intratelomeric reads

516 normalized by the total number of reads with a GC composition like that of telomeres. Telomeric

517 enrichment in tumours was defined as a $\log_2$ ratio of tumour telomere content to blood telomere content

518 greater than 0.5. TelomereHunter was also applied to WTS for each tumour to estimate TERRA content.

519

Mutational signature analysis

For each sample, the single base substitution (SBS), doublet base substitution (DBS), and small insertions and deletions (ID) mutation count matrices were extracted from variant call format (VCF) files containing somatic variant calls using the *MutationalPatterns* (version 3.10.0)[77] package for R. The optimal linear combination of the COSMIC V3[78] SBS, DBS, and ID mutational signatures that best reconstructed their respective profiles was then estimated using the *fit_to_signatures* function.

Microsatellite instability assessment

Insertions and deletions in microsatellite regions were assessed using *PURPLE* (version 3.1). Samples with more than four microsatellite Indels per megabase were considered to have microsatellite instability as per the software default setting.

Identification of recurrent copy number alterations

The Genomic Identification of Significant Targets in Cancer (GISTIC, version 2.0)[79] algorithm was used to identify recurrent copy alterations. The input data for GISTIC was modified from the somatic segmentation output from PURPLE by taking log2 of the segmental copy number incremented by a small offset (0.01) and subtracting one to center the diploid state around zero (log2(CN + 0.01)-1). GISTIC was run in broad mode with segments containing less than 50 markers undergoing joining. The broad length cutoff was set to 75% of a chromosome and arm-peel was activated. The analysis was applied independently to sample subsets including HN-PG/parasympathetic PG, non-metastatic and metastatic sympathetic PCPG. In cases where a patient had more than one primary tumour, one was chosen at random, in cases where a paired primary and metastasis were present, the metastasis was used.

Identification of driver genes

The dNdScv R package[33] was used to assess somatic mutations to detect genes under positive selection. Before running the analysis, quality filtered somatic variant calls were lifted over from the GRCh38 to HG19 genome build using the *rtracklayer* package for R with a liftover chain obtained from UCSC (hg38ToHg19.over.chain). The resulting mutation set was analysed with *dndscv* function using default parameters. Additionally, the HG19 mutation set was used to run the OncodriveFML[34] driver detection tool via the web-based application interface (https://bbglab.irbbarcelona.org/oncodrivefml/home, accessed 5th February 2024). The algorithm was run using genomic region subsets encompassing coding sequences or promotor regions with Combined Annotation Dependent Depletion (CADD) scores version 1.0.

RNA-Seq

Library preparation

Samples were prepared using the NEB-Next directional RNA-Seq kit (NEB, USA) and underwent 150bp paired-end sequencing on the Illumina NovaSeq 6000 (Illumina, USA) according to manufacturer's instructions.

Read quantification

RNA sequencing reads were aligned with *STAR*[80] (version 2.7.9a) using a two pass approach. First, all data was aligned using a *STAR* reference built with the Gencode human reference genome with decoy HLA sequences (GRCh38) and Gencode gene transcript annotation file (version 36, primary assembly annotation). Following alignment, the splice junction output from all samples was merged. Supporting read evidence for each junction was summed and junctions with less than 10 unique supporting reads were removed. The resulting junction file was used to build a new *STAR* reference and the alignment was repeated. Gene level feature counts were obtained with *HTSeq-count* (version 0.11.3) using the previously described Gencode transcript annotation file. All parameters were default except mode which was set to intersection-nonempty.

Differential gene expression

To contrast gene expression between parasympathetic and sympathetic (including pheochromocytoma) paraganglioma, samples were assigned to one of two groups based on clinical annotation and UMAP clustering. Samples where UMAP clustering did not reflect the clinical annotation or tumour purity was below 50% were excluded from the contrast. To perform differential expression analysis, transcript counts obtained from HTSeq-count were converted to a digital gene expression object using the *edgeR* (version 3.42.4)[81] package for R. Lowly expressed genes were removed using the *filterByExpr* function with default parameters. Library scaling factors were then computed using the *calcNormFactors* function. A design matrix was constructed without an intercept to include the differential group and patient gender as a covariate. Normalization factors were applied and correction weights for count-dependent variance were computed using the *voom* function from the *limma*[82] (version 3.56.2) package for R. To account for multiple samples from the same patient, the inter-duplicate correlation was computed using the *duplicateCorrelation* function with the patient identifier as the blocking factor. Linear model fitting was performed using the *lmFit* function supplied with the duplicate correlation computed above and the patient identifier as the blocking variable. Contrasts were fitted using the *contrasts.fit* function and test-statistics were computed using the *eBayes* function.

To contrast metastatic, *TERT*-altered, and *ATRX*-altered tumours with non-metastatic primary tumours samples were assigned to groups based on clinical behaviour. The clinical behaviour groups were non-

589 metastatic primary tumour, primary tumour where metastatic disease was present, metastatic lesion, or a

590 tumour with short clinical follow up. These groups were then further segregated based on the presence or

591 absence of a *TERT* or *ATRX* mutation. Parasympathetic tumours and tumours with low purity (<50%) were

592 excluded from all the contrasts. Samples with an *ATRX/TERT* alterations where the allele fraction was less

593 than 25% were excluded from genotype-centric contrasts, and samples with short clinical follow-up were

594 excluded from contrasts involving clinical behaviour. See Supplementary Data 2 for a full list of contrast

595 participation. Differential expression was performed as described above.

596

597 **RNA fusion detection**

598 Whole transcriptome sequencing data aligned with STAR aligner (described above) was analysed with the

599 *Arriba* (version 2.1.0) gene fusion detection tool using the supplied blacklist, known fusion, and protein

600 domain files with default parameters.

601

602 **Harmonization with published RNA-seq datasets**

603 Read counts previously published by Fishbein et al. were obtained from the Genomic Data Commons using

604 the TCGAbiolinks[83] (version 2.29.1) package for R with these parameters: project = "TCGA-PCPG",

605 data.category = "Transcriptome Profiling", data.type = "Gene Expression Quantification", workflow.type =

606 "STAR - Counts". Additional data previously published by Flynn et al[14] was obtained from the European

607 Genome-Phenome Archive (EGAS00001005861). Raw counts from the publicly available data were merged

608 with our dataset retaining genes present in all three datasets. Count matrices were converted to a digital

609 gene expression object with *edgeR and l*owly expressed genes were removed using the *filterByExpr* function

610 with default parameters. Library scaling factors were then computed using the *calcNormFactors* function

611 and counts were transformed to log counts per million using the *cpm* function. Possible technical variance

612 was ameliorated using the *removeBatchEffect* function from the *limma* package where the dataset identifier

613 was supplied as the batch and the primary driver genotype (e.g RET, SHDx, VHL) as the factor to preserve.

614

615 **Small RNA-Seq**

616

617 **Library preparation**

618 Samples were prepared using the NEXTFLEX® Small RNA-Seq Kit v3 (Bioo Scientific). Samples were

619 sequenced at the molecular genomics core (Peter MacCallum Cancer Centre) using 50bp single end

620 sequencing on the Illumina NextSeq 500 (Illumina, USA).

621

622 **Read quantification**

623 FASTQ files were pre-processed with two rounds of *cutadapt* (version 1.6.3) to first remove adapter

624 sequences (-a TGGAATTCTCGGGTGCCAAGG, --minimum-length 23) and then remove the first and last

625 four bases (-u 4, -u -4). Following trimming, sequences were aligned to GRCh38 with *subread* (version

626 1.6.3) and quantified using *featurecounts* (version 1.6.3) in stranded mode against the miRBase (version 20)

627 miRNA transcripts[84]. Following read quantification, read-count processing was performed in an identical

628 manner to that described under RNA-Seq analysis.

629

Harmonization with published small-RNA-seq datasets

631 Small-RNA sequencing data previously published by Castro-Vega et al were obtained from ArrayExpress

632 (E-MTAB-2833, https://www.ebi.ac.uk/arrayexpress/experiments/E-MTAB-2833). Additional data

633 published by Fishbein et al. were downloaded from the Genomic Data Commons using the GDC Data

634 Transfer Tool in BAM format and converted to FASTQ format using SAMtools (1.10). Alignment and read

635 quantification was performed as described above under 'Read quantification'. Read count harmonization

636 was performed as described for RNA-seq dataset under 'Harmonization with published RNA-seq datasets'.

637

Methylation analysis

639 Methylation profiling was performed by the Australian Genome Research Facility (AGRF). Tumour DNA

640 samples were normalized to approximately 200ng of DNA in 45µL. Bisulfite conversion was performed

641 with the EZ-96 DNA Methylation MagPrep (Zymo Research, California, USA). Bisulfite converted DNA

642 was processed on the Illumina Human Methylation EPIC BeadChip (Illumina, California, USA) following

643 the Illumina Infinium HD Methylation assay protocol (AGRF NATA scope GGTMN00263)

644

Methylation array data pre-processing and normalization

646 The *minfi* (version 1.46.0) package for R was used to read in a targets manifest and red/green channel IDAT

647 files using the *read.metharray.sheet* and *read.metharray.exp* functions, respectively. Probe detection p-

648 values were determined with the *detectionP* function. Raw green/red values were converted to methylation

649 signal and functionally normalized using the *preprocessFunnorm* function from *minfi*. Any probes with a

650 detection p-value below 0.01 in any sample or those that fell on a SNP position (using *dropLociWithSnps*)

651 were removed from the dataset. Furthermore, the *maxprobes* package for R was used to exclude any cross-

652 reactive probes. Illumina probe annotation version 1.0 with GRCh38 coordinate information was obtained

653 from: https://github.com/achilleasNP/IlluminaHumanMethylationEPICanno.ilm10b5.hg38

654

Probe level differential expression

656 Probe level differential methylation analysis was performed using the Remove Unwanted Variation

657 workflow with the RUV package via the *MissMethyl* package for R[85,86]. Firstly, functionally normalized

658 methylation values were converted to M-values using the *getM* function from the *minfi* package and

659 negative control probes were obtained using the *MissMethyl*'s *getINCs* function. For each contrast, two

660 rounds of variation adjustment were performed. In the first round, an RUV model was computed with RUV-

661 inverse algorithm using the *RUVfit* function applied using the Illumina negative control probes as controls.

662 The rescaled variances were then applied using the *RUVadj* function and p-values for differential

663   methylation of each probe were obtained with the *topRUV* function. Probes with a p-value greater than 0.5

664   were selected for use as controls in the second round of variation adjustment using the RUVfit function and

665   the resulting model was applied using the *RUVadj* function.

666

Differentially methylated regions

668   Identification of differentially methylated regions was performed with the DMRcate[87] package (version

669   2.14.1) for R. Firstly, functionally normalized methylation values were converted to M-values using the

670   *getM* function from the *minfi* package. Contrast and design matrices were generated using the same process

671   described for differential gene expression. For each contrast, individual probes were then annotated using

672   the *cpg.annotate* function with analysis type set to differential and the default annotation set for Illumina

673   EPIC arrays (ilm10b2.hg19). Differentially methylated regions were then identified using the *dmrcate*

674   function with a lambda of 1000 and bandwidth scaling factor of 2. Significant DMRs were those with a

675   Fisher multiple comparison statistic below 0.05.

676

Harmonization with previously published methylation array datasets

678   Illumina Infinium HumanMethylation450 methylation array data previously made available by Fishbein et

679   al. were obtained from the Genomic Data Commons using the TCGAbiolinks[83] (version 2.29.1) package for

680   R with these parameters: project = "TCGA-PCPG", data.category = "DNA Methylation", data.format =

681   "IDAT", legacy = False. The array data were processed as described under 'Methylation array data pre-

682   processing and normalization' with the exception of the annotation file, which was substituted with the

683   supplied Illumina Infinium HumanMethylation450 annotation. Additional data made available by Letouzé et

684   al.[9] were obtained from the Gene Expression Omnibus using the GEOquery package for R (accession

685   GSE39198 and GSE43293). The GSE39198/GSE43293 data was only available as beta values and was not

686   reprocessed. The beta-values from all three datasets were converted to m-values and merged, retaining only

687   probes available on the Illumina Infinium HumanMethylation27 array design. A design matrix was

688   generated with the *model.matrix* function from the limma package using the primary driver genotype (e.g.

689   RET, SHDx, VHL, Unknown). Batch effects were then adjusted using the *removeBatchEffect* function from

690   limma where the dataset was supplied as the first batch annotation and patient gender as the second batch

691   annotation.

692

Single nuclei RNA-sequencing

694

Library preparation with 10x Chromium

696   snRNA-seq was performed using the 'Frankenstein' protocol (dx.doi.org/10.17504/protocols.io.bqxymxpw).

697   Briefly, nuclei were extracted from frozen tissues and subjected to fluorescence-activated nuclei sorting

698   (FANS) using 4′,6-diamidino-2-phenylindole (DAPI). Sorting was performed using a BD FACSaria 2

699   instrument, sorting between 3000 and 10,000 nuclei per sample, capturing both diploid and tetraploid

populations. FAN-sorted nuclei were immediately processed using either the 10x Chromium Single Cell 5'
(PN-1000006, 4 samples) or 3' (PN-1000075, 4 samples) Library & Gel Bead Kit (10x Genomics, USA).
Once processed, snRNA-seq libraries were sequenced on the Illumina Nova-Seq 6000 (Illumina, USA)
using 150bp paired-end sequencing.

Data processing and analysis
Additional snRNA-seq data for two normal adrenal medulla samples (E240, E243) previously published by
Zethovan et al.[22] were obtained from the European-genome-phenome archive (accession
EGAS00001005861). Single-nuclei RNA sequencing reads in FASTQ format were aligned and counted
using *CellRanger* (version 7.2.0). Read-one data for libraries processed with the 3' protocol were restricted
to the first 26 bases using the r1-length flag. Feature counting was performed using the 10x supplied
GRCh38 transcriptome (version refdata-gex-GRCh38-2020-A) with reads aligning to introns contributing to
feature counts. Single-Cell Remover of Doublets (SCRUBLET, version 0.2.3) was used to identify gel-
beads containing more than one cell. CellRanger count matrices were loaded using the *Read10X* and
CreateSeuratObject functions from the Seurat (version 4.3.0.1) package for R in conjunction with the
SCRUBLET output. For each sample, features present in less than three cells and cells containing less than
500 features or 750 unique RNA molecules, or more than 10 percent mitochondrial RNA were excluded.
Cell cycle scoring was performed on normalized and scaled counts using the S-phase and G2M-phase
marker gene lists provided with the Seurat package. The data was scaled again using *ScaleData* function
with S-phase score, G2M-phase score, unique RNA molecule count, and percent mitochondrial RNA
supplied as regression variables. Cell type clusters were found using the *FindClusters* function and cell types
were assigned manually using marker genes for fibroblast (*FAP, PDGFRB, PDGFRA, ACTA2, COL1A1*),
chromaffin (*PNMT, TH, DBH, CHGA, CHGB*), adrenocortical (*STAR, CYP11B1, CYP11A1*), endothelial
(*FLT1, EPAS1*), sustentacular (*CDH19, SOX10, S100B, VIM*), monocyte/macrophage (*MSR1, CD163,
CCL3*), and lymphocyte (*CD2, CD3E , MS4A1*) cell types.

Single nuclei ATAC-sequencing

Library preparation with 10x Chromium
snATAC-seq was conducted using the "Van Helsing" protocol
(dx.doi.org/10.17504/protocols.io.bw52pg8e). Initially, nuclei were isolated following the steps outlined in
the previously mentioned "Frankenstein" protocol. Sorted nuclei were collected into a round-bottom 96-well
plate containing 100 µL of ice-cold Wash Buffer. The sorted nuclei were then transferred to 0.2 mL PCR
tubes; 50 µL of ATAC Wash Buffer-Dig was added to the well to ensure transfer of any remaining nuclei.
The nuclei were then centrifuged at 500xg for 5 minutes at 4°C. The supernatant was carefully decanted,
leaving behind approximately 10 µL. Without resuspending the pellet, 100 µL of ice-cold Diluted Nuclei
Buffer was added. The sample was centrifuged again under the same conditions, and 100 µL of the

737   supernatant was gently removed in two steps—first 90 µL, then the remaining 10 µL. Another 100 µL of

738   Diluted Nuclei Buffer was added gently. This washing step was repeated, removing the supernatant in two

739   steps to leave behind approximately 7-10 µL. The nuclei were resuspended in this small volume, ensuring

740   thorough mixing by carefully washing the walls of the tube. For quantification, 1-2 µL of the nuclei

741   suspension was diluted 1:5 with Diluted Nuclei Buffer and mixed 1:1 with Trypan Blue. Nuclei were

742   counted using a Countess II FL Automated Cell Counter or a hematocytometer to estimate the expected

743   number of nuclei based on the recovery factor. Finally, 5 µL of the nuclei suspension in Diluted Nuclei

744   Buffer were used directly in the Chromium Single Cell ATAC Reagent Kits protocol (CG000168 Rev A),

745   following the specific recommendations for low input samples to optimize the transposition reaction and

746   subsequent library preparation.. Once processed, snATAC-seq libraries were sequenced on the Illumina

747   NextSeq 500 (Illumina, USA) using 50bp paired-end, duel-indexed sequencing.

748

749   **Data preprocessing**

750   Raw sequencing data was demultiplexed using *cellranger-atac mkfastq* (V2.0.0). *Cellranger-atac count* was

751   used to combine replicate sequencing runs, align single nuclei ATAC reads to the GRCh38 reference

752   genome (GRCh38 2020 A 2.0.0, 10x Genomics), and call initial peak sets for individual samples.

753   *Cellranger-atac aggr* was then used to combine samples into a single peak-barcode matrix.

754

755   **Quality control**

756   Signac[88] (version 1.12.9004) and Seurat (version 4.3.0.1) were used for quality control and downstream

757   analysis of snATAC-seq data. Filters were applied to QC metrics that were independent of peaks, to avoid

758   bias toward under-represented cell types. Transcription start site enrichment scores were calculated using the

759   *Signac TSSEnrichment* function. Outlier nuclei with over 5000 unique reads were assumed to be doublets or

760   nuclei clumps and removed. Nuclei with TSS enrichment scores below 2 were removed due to having a low

761   signal-to-noise ratio.

762

763   **Cell type identification**

764   Cell type identification was performed via label transfer in Signac. A gene-by-cell accessibility matrix was

765   computed by calculating the sum of reads aligning to the gene body and promoter regions of protein-coding

766   genes for each cell. Log normalisation was performed on the gene activities with *Seurat NormalizeData*.

767   Integration was performed to link snATAC-seq nuclei clusters to defined cell types within the snRNA-seq

768   dataset generated from matched and similar samples[89]. Integration was performed with the

769   *FindTransferAnchors* Seurat function. Briefly, Canonical Correlation Analysis (CCA) was used to identify

770   shared sources of variation between the snATAC gene activity and snRNA gene expression, and project the

771   two datasets into the same reduced-dimensional space. Mutual nearest neighbours (cell pairs from each

772   dataset within each other's neighbourhood) were identified and used as integration anchors between the two

773   datasets. These anchors were then used to transfer cell-type labels from the snRNA reference dataset to the

to snATAC-seq dataset, using the Seurat *TransferData* function, enabling prediction of snATAC-seq nuclei cell types. Cell type identification was confirmed by gene activity of canonical cell-type-specific marker genes.

Peak calling and visualisation

Open genomic regions were defined using pooled reads for each cell type and tumour sample with > 100 total nuclei individually using the MACS2[90] peak caller (version 2.2.9.1) implemented in the Signac *CallPeaks* function. Resultant fragment pileup bedgraph files for each cell type were visualized using the SparK command line tool[91].

Cell-Free DNA panel sequencing

Sample collection
Patient blood was collected in Cell Free DNA BCT CE tubes (catalogue number 218996, Streck, USA). Within 2 hours of collection, whole blood was centrifuged at 1900g (brake off) for ten minutes to separate the plasma. Plasma was aspirated and aliquots were centrifuged at 20000g to pellet residual cells or debris. The plasma was stored at -80°C until DNA extraction. Cell free DNA (cfDNA) was extracted from 5mL of plasma using the Qiagen QIAamp circulating nucleic acid kit (catalogue number 55114, Qiagen, The Netherlands) according to manufacturer's instructions.

Library preparation
A sequencing library was generated with 30ng of input cfDNA using the Illumina TruSightOncology 500 ctDNA library preparation kit (catalogue number 20039252, Illumina, USA). Input quantity was determined based on the mononucleosome fraction (75-300bp) using the Agilent TapeStation4200. Library preparation was performed as per manufacturer's instructions with the addition of a 1.2x bead clean-up of the amplified enriched library. The fragment distribution of the enriched library was assessed on the TapeStation4200, and library quantification was performed using the KAPA Illumina library quantification kit (catalogue number 07960140001, Roche, Switzerland) and analysed with QuantStudio6 (ThermoFisher, USA).

Sequencing and data processing
Sequencing was performed at the University of Melbourne Centre for Cancer Research Centre using the Illumina NovaSeq 6000 (Illumina, USA) to achieve a depth of coverage greater than 35000x. Data was analysed with Illumina DRAGEN TruSight Oncology 500 ctDNA Analysis Software v1.2 on the Illumina Connected Analytics platform (ICA v1). PierianDx Clinical Genomics Workspace (v6.27.0.1) was used for variant interpretation.

Immunohistochemistry

Immunohistochemistry was performed and interpreted on formalin fixed paraffin embedded tissue sections using methods that have been described in detail elsewhere [92,93]. Briefly, for both SDHB (ABCAM, Cambridge, UK: ab14714, clone 21A11, dilution 1:100) and Ki67 (clone M7240 Dako, Carpenteria, CA USA, dilution 1:50) commercially available mouse monoclonal antibodies were used.

C-Circle Assay

Isothermal rolling circle amplification and detection of C-circles was performed as described [40,94]. For each tumour sample, 20 ng DNA was incubated with 10 μl 0.2 mg/ml bovine serum albumin, 0.1% Tween, 4 mM DTT, 1 mM each dATP, dGTP, dCTP and dTTP, 1× Φ29 Buffer , with or without Φ29 polymerase 7.5 U (New England Biolabs) at 30 °C for 8 hours, then at 65 °C for 20 min. Reaction products were diluted to 100 μl with 2× SSC and dot-blotted onto a 2× SSC-soaked Biodyne B nylon membrane (Pall Corporation). The membrane was air-dried, twice crosslinked using 1,200 J UV (Stratagene) and hybridized overnight at 37°C with end-labelled 32P-(CCCTAA)3 and PerfectHyb Plus hybridization buffer (Sigma). The membrane was then washed at 37°C three times in 0.5x SSC/0.1% SDS and exposed to a storage phosphor screen, which was imaged using an AmershamTM TyphoonTM laser scanner (Cytiva) and analysed by densitometry using ImageQuant software (Molecular Dynamics). C-Circle levels for each tumour sample were reported as the difference in the dot-blot intensities resulting from reaction of the sample's DNA with and without Φ29 polymerase.

Statistical analysis

Student's t-tests and Pearson's Chi-squared tests for count data were performed using the *t.test* and *chisq.test* functions, respectively, from the base *stats* package for R (version 4.3.1)

Data availability

Raw FASTQ files for WGS, WTS, small-RNA-sequencing, sn-ATAC-sequencing, sn-RNA-sequencing, as well as GRCh38 aligned CRAM files for WGS, and IDAT files for Illumina EPIC methylation array profiling are available from the European-genome-phenome (EGA) archive (EGASxxxxxxxxx, pending) under restricted access and controlled by the Data Access Committee at the University of Melbourne Centre for Cancer Research. A data package containing non-identifiable data from tertiary analysis including somatic small and structural variant calls, copy-number analysis, RNA-fusion calls, and gene expression matrices from bulk and single nuclei analysis are available from Figshare (https://doi.org/10.6084/m9.figshare.25792479). RNA-seq, Illumina Infinium HumanMethylation450 arrays, and small-RNA-seq data previously made available by Fishbein et al. was obtained from the National Computational Infrastructure's Genomic Data Commons. Bulk RNA-seq data previously published by Flynn et al. and snRNA data published by Zethoven et al. was obtained from EGA (EGAS00001005861

847 [https://ega-archive.org/studies/EGAS00001005861]). Small-RNA-seq previously published by Castro-Vega

848 et al were obtained from ArrayExpress (E-MTAB-2833 [https://www.ebi.ac.uk/arrayexpress/experiments/E-

849 MTAB-2833]). Illumina Infinium HumanMethylation450 and HumanMethylation27 arrays previously made

850 available by Letouzé et al. were obtained from the Gene Expression Omnibus (accession GSE39198

851 [https://www.ncbi.nlm.nih.gov/geo/query/acc.cgi?acc=GSE39198], and GSE43293

852 [https://www.ncbi.nlm.nih.gov/geo/query/acc.cgi?acc=GSE43293])

853

854 **Code availability**

855 All code used in the generation and analysis of data contained within this publication are available from

856 GitHub: https://github.com/UMCCR-RADIO-Lab/a5_sdhb_pcpg

857

858 **References**

859

860 1.   Nazari, M.A.*, et al.* Catecholamine-induced hypertensive crises: current insights and management.
861   *Lancet Diabetes Endocrinol* **11**, 942-954 (2023).
862 2.   Lenders, J.W., Eisenhofer, G., Mannelli, M. & Pacak, K. Phaeochromocytoma. *Lancet* **366**, 665-675
863   (2005).
864 3.   Ayala-Ramirez, M.*, et al.* Clinical risk factors for malignancy and overall survival in patients with
865   pheochromocytomas and sympathetic paragangliomas: primary tumor size and primary tumor
866   location as prognostic indicators. *J Clin Endocrinol Metab* **96**, 717-725 (2011).
867 4.   Lenders, J.W.M.*, et al.* Genetics, diagnosis, management and future directions of research of
868   phaeochromocytoma and paraganglioma: a position statement and consensus of the Working
869   Group on Endocrine Hypertension of the European Society of Hypertension. *Journal of hypertension*
870   **38**, 1443-1456 (2020).
871 5.   Amar, L.*, et al.* International consensus on initial screening and follow-up of asymptomatic SDHx
872   mutation carriers. *Nat Rev Endocrinol* **17**, 435-444 (2021).
873 6.   Davidoff, D.F.*, et al.* Surveillance Improves Outcomes for Carriers of SDHB Pathogenic Variants: A
874   Multicenter Study. *J Clin Endocrinol Metab* **107**, e1907-e1916 (2022).
875 7.   Selak, M.A.*, et al.* Succinate links TCA cycle dysfunction to oncogenesis by inhibiting HIF-alpha prolyl
876   hydroxylase. *Cancer Cell* **7**, 77-85 (2005).
877 8.   Xiao, M.*, et al.* Inhibition of alpha-KG-dependent histone and DNA demethylases by fumarate and
878   succinate that are accumulated in mutations of FH and SDH tumor suppressors. *Genes Dev* **26**,
879   1326-1338 (2012).
880 9.   Letouze, E.*, et al.* SDH mutations establish a hypermethylator phenotype in paraganglioma. *Cancer*
881   *Cell* **23**, 739-752 (2013).
882 10.   Liu, T.*, et al.* The activating TERT promoter mutation C228T is recurrent in subsets of adrenal
883   tumors. *Endocr Relat Cancer* **21**, 427-434 (2014).
884 11.   Calsina, B.*, et al.* Genomic and immune landscape Of metastatic pheochromocytoma and
885   paraganglioma. *Nat Commun* **14**, 1122 (2023).
886 12.   Fishbein, L.*, et al.* Whole-exome sequencing identifies somatic ATRX mutations in
887   pheochromocytomas and paragangliomas. *Nat Commun* **6**, 6140 (2015).
888 13.   Fishbein, L.*, et al.* Comprehensive Molecular Characterization of Pheochromocytoma and
889   Paraganglioma. *Cancer Cell* **31**, 181-193 (2017).
890 14.   Flynn, A.*, et al.* The genomic landscape of phaeochromocytoma. *J Pathol* **236**, 78-89 (2015).
891 15.   Job, S.*, et al.* Telomerase activation and ATRX mutations are independent risk factors for metastatic
892   pheochromocytoma and paraganglioma. *Clin Cancer Res* (2018).

893 16. Dwight, T*., et al.* TERT structural rearrangements in metastatic pheochromocytomas. *Endocr Relat*
894 *Cancer* **25**, 1-9 (2018).
895 17. Dahia, P.L*., et al.* A HIF1alpha regulatory loop links hypoxia and mitochondrial signals in
896 pheochromocytomas. *PLoS Genet* **1**, 72-80 (2005).
897 18. Burnichon, N*., et al.* Integrative genomic analysis reveals somatic mutations in pheochromocytoma
898 and paraganglioma. *Hum Mol Genet* **20**, 3974-3985 (2011).
899 19. Castro-Vega, L.J*., et al.* Germline mutations in FH confer predisposition to malignant
900 pheochromocytomas and paragangliomas. *Hum Mol Genet* **23**, 2440-2446 (2014).
901 20. Castro-Vega, L.J*., et al.* Multi-omics analysis defines core genomic alterations in
902 pheochromocytomas and paragangliomas. *Nat Commun* **6**, 6044 (2015).
903 21. Comino-Mendez, I*., et al.* Exome sequencing identifies MAX mutations as a cause of hereditary
904 pheochromocytoma. *Nat Genet* **43**, 663-667 (2011).
905 22. Zethoven, M*., et al.* Single-nuclei and bulk-tissue gene-expression analysis of pheochromocytoma
906 and paraganglioma links disease subtypes with tumor microenvironment. *Nat Commun* **13**, 6262
907 (2022).
908 23. Turchini, J., Cheung, V.K.Y., Tischler, A.S., De Krijger, R.R. & Gill, A.J. Pathology and genetics of
909 phaeochromocytoma and paraganglioma. *Histopathology* **72**, 97-105 (2018).
910 24. Kameneva, P*., et al.* Single-cell transcriptomics of human embryos identifies multiple sympathoblast
911 lineages with potential implications for neuroblastoma origin. *Nat Genet* **53**, 694-706 (2021).
912 25. Eisenhofer, G*., et al.* Biochemical and clinical manifestations of dopamine-producing
913 paragangliomas: utility of plasma methoxytyramine. *J Clin Endocrinol Metab* **90**, 2068-2075 (2005).
914 26. Richter, S*., et al.* Head/neck paragangliomas: focus on tumor location, mutational status and
915 plasma methoxytyramine. *Endocr Relat Cancer* **29**, 213-224 (2022).
916 27. Fottner, C*., et al.* 6-18F-fluoro-L-dihydroxyphenylalanine positron emission tomography is superior
917 to 123I-metaiodobenzyl-guanidine scintigraphy in the detection of extraadrenal and hereditary
918 pheochromocytomas and paragangliomas: correlation with vesicular monoamine transporter
919 expression. *J Clin Endocrinol Metab* **95**, 2800-2810 (2010).
920 28. Taieb, D., Jha, A., Treglia, G. & Pacak, K. Molecular imaging and radionuclide therapy of
921 pheochromocytoma and paraganglioma in the era of genomic characterization of disease
922 subgroups. *Endocr Relat Cancer* **26**, R627-R652 (2019).
923 29. Yokoyama, T., Misuzu, Y.Y. & Yamamoto, Y. Immunohistochemical localization of tryptophan
924 hydroxylase and serotonin transporter in the carotid body of the rat. *Histochem Cell Biol* **140**, 147-
925 155 (2013).
926 30. van Hulsteijn, L.T., van Duinen, N., Romijn, J.A., Smit, J.W. & Corssmit, E.P. Urinary 5-HIAA excretion
927 is not increased in patients with head and neck paragangliomas. *Int J Biol Markers* **27**, e160-163
928 (2012).
929 31. Kimura, N*., et al.* Immunohistochemical Expression of Choline Acetyltransferase and
930 Catecholamine-Synthesizing Enzymes in Head-and-Neck and Thoracoabdominal Paragangliomas
931 and Pheochromocytomas. *Endocr Pathol* **32**, 442-451 (2021).
932 32. Tamborero, D*., et al.* Cancer Genome Interpreter annotates the biological and clinical relevance of
933 tumor alterations. *Genome Med* **10**, 25 (2018).
934 33. Martincorena, I*., et al.* Universal Patterns of Selection in Cancer and Somatic Tissues. *Cell* **171**,
935 1029-1041 e1021 (2017).
936 34. Mularoni, L., Sabarinathan, R., Deu-Pons, J., Gonzalez-Perez, A. & Lopez-Bigas, N. OncodriveFML: a
937 general framework to identify coding and non-coding regions with cancer driver mutations.
938 *Genome Biol* **17**, 128 (2016).
939 35. Yang, C*., et al.* Novel HIF2A mutations disrupt oxygen sensing, leading to polycythemia,
940 paragangliomas, and somatostatinomas. *Blood* **121**, 2563-2566 (2013).
941 36. Welander, J*., et al.* Rare germline mutations identified by targeted next-generation sequencing of
942 susceptibility genes in pheochromocytoma and paraganglioma. *J Clin Endocrinol Metab* **99**, E1352-
943 1360 (2014).

944	37.	Pang, Y*., et al.* Nonmosaic somatic HIF2A mutations associated with late onset polycythemia-
945		paraganglioma syndrome: Newly recognized subclass of polycythemia-paraganglioma syndrome.
946		*Cancer* **125**, 1258-1266 (2019).

944 37. Pang, Y*., et al.* Nonmosaic somatic HIF2A mutations associated with late onset polycythemia-
945 paraganglioma syndrome: Newly recognized subclass of polycythemia-paraganglioma syndrome.
946 *Cancer* **125**, 1258-1266 (2019).

947 38. Wilzen, A*., et al.* Malignant pheochromocytomas/paragangliomas harbor mutations in transport
948 and cell adhesion genes. *Int J Cancer* **138**, 2201-2211 (2016).

949 39. Bell, R.J*., et al.* Cancer. The transcription factor GABP selectively binds and activates the mutant
950 TERT promoter in cancer. *Science* **348**, 1036-1039 (2015).

951 40. Henson, J.D*., et al.* DNA C-circles are specific and quantifiable markers of alternative-lengthening-
952 of-telomeres activity. *Nat Biotechnol* **27**, 1181-1185 (2009).

953 41. Sieverling, L*., et al.* Genomic footprints of activated telomere maintenance mechanisms in cancer.
954 *Nat Commun* **11**, 733 (2020).

955 42. Jang, S.H., Kim, A.R., Park, N.H., Park, J.W. & Han, I.S. DRG2 Regulates G2/M Progression via the
956 Cyclin B1-Cdk1 Complex. *Mol Cells* **39**, 699-704 (2016).

957 43. Nolting, S*., et al.* Personalized Management of Pheochromocytoma and Paraganglioma. *Endocr Rev*
958 **43**, 199-239 (2022).

959 44. Kitange, G.J*., et al.* Induction of MGMT expression is associated with temozolomide resistance in
960 glioblastoma xenografts. *Neuro Oncol* **11**, 281-291 (2009).

961 45. Alexandrov, L.B*., et al.* Signatures of mutational processes in human cancer. *Nature* **500**, 415-421
962 (2013).

963 46. Touat, M*., et al.* Mechanisms and therapeutic implications of hypermutation in gliomas. *Nature*
964 **580**, 517-523 (2020).

965 47. Backman, S*., et al.* The Evolutionary History of Metastatic Pancreatic Neuroendocrine Tumours
966 Reveals a Therapy Driven Route to High-Grade Transformation. *medRxiv*,
967 2024.2001.2008.24300723 (2024).

968 48. Hanahan, D. & Weinberg, R.A. Hallmarks of cancer: the next generation. *Cell* **144**, 646-674 (2011).

969 49. Kim, N.W*., et al.* Specific association of human telomerase activity with immortal cells and cancer.
970 *Science* **266**, 2011-2015 (1994).

971 50. Dagg, R.A*., et al.* Extensive Proliferation of Human Cancer Cells with Ever-Shorter Telomeres. *Cell*
972 *Rep* **19**, 2544-2556 (2017).

973 51. Hiraga, S*., et al.* Telomerase activity and alterations in telomere length in human brain tumors.
974 *Cancer Res* **58**, 2117-2125 (1998).

975 52. Thompson, C.A.H. & Wong, J.M.Y. Non-canonical Functions of Telomerase Reverse Transcriptase:
976 Emerging Roles and Biological Relevance. *Curr Top Med Chem* **20**, 498-507 (2020).

977 53. Kimura, N*., et al.* Pathological grading for predicting metastasis in phaeochromocytoma and
978 paraganglioma. *Endocr Relat Cancer* **21**, 405-414 (2014).

979 54. Qin, T*., et al.* ATRX loss in glioma results in dysregulation of cell-cycle phase transition and ATM
980 inhibitor radio-sensitization. *Cell Rep* **38**, 110216 (2022).

981 55. Ohki, R*., et al.* Reprimo, a new candidate mediator of the p53-mediated cell cycle arrest at the G2
982 phase. *J Biol Chem* **275**, 22627-22630 (2000).

983 56. Li, Y*., et al.* Non-canonical NF-kappaB signalling and ETS1/2 cooperatively drive C250T mutant TERT
984 promoter activation. *Nat Cell Biol* **17**, 1327-1338 (2015).

985 57. Cao, Y., Li, H., Deb, S. & Liu, J.P. TERT regulates cell survival independent of telomerase enzymatic
986 activity. *Oncogene* **21**, 3130-3138 (2002).

987 58. Khattar, E*., et al.* Telomerase reverse transcriptase promotes cancer cell proliferation by
988 augmenting tRNA expression. *J Clin Invest* **126**, 4045-4060 (2016).

989 59. Liang, J*., et al.* Genome-Wide CRISPR-Cas9 Screen Reveals Selective Vulnerability of ATRX-Mutant
990 Cancers to WEE1 Inhibition. *Cancer Res* **80**, 510-523 (2020).

991 60. Garbarino, J., Eckroate, J., Sundaram, R.K., Jensen, R.B. & Bindra, R.S. Loss of ATRX confers DNA
992 repair defects and PARP inhibitor sensitivity. *Transl Oncol* **14**, 101147 (2021).

993 61. George, S.L*., et al.* Therapeutic vulnerabilities in the DNA damage response for the treatment of
994 ATRX mutant neuroblastoma. *EBioMedicine* **59**, 102971 (2020).

995 62. Cullinane, C.*, et al.* Enhancing the anti-tumour activity of (177)Lu-DOTA-octreotate radionuclide
996   therapy in somatostatin receptor-2 expressing tumour models by targeting PARP. *Sci Rep* **10**, 10196
997   (2020).
998 63. Waldeck, K.*, et al.* A genome-wide CRISPR/Cas9 screen identifies DNA-PK as a sensitiser to
999   (177)Lutetium-DOTA-octreotate radionuclide therapy. *Theranostics* **13**, 4745-4761 (2023).
000 64. Chan, E.M.*, et al.* WRN helicase is a synthetic lethal target in microsatellite unstable cancers. *Nature*
001   **568**, 551-556 (2019).
002 65. Kamihara, J.*, et al.* Belzutifan, a Potent HIF2alpha Inhibitor, in the Pacak-Zhuang Syndrome. *N Engl J*
003   *Med* **385**, 2059-2065 (2021).
004 66. Robinson, J.T.*, et al.* Integrative genomics viewer. *Nat Biotechnol* **29**, 24-26 (2011).
005 67. Didion, J.P., Martin, M. & Collins, F.S. Atropos: specific, sensitive, and speedy trimming of
006   sequencing reads. *PeerJ* **5**, e3720 (2017).
007 68. Li, H. & Durbin, R. Fast and accurate short read alignment with Burrows-Wheeler transform.
008   *Bioinformatics* **25**, 1754-1760 (2009).
009 69. Lai, Z.*, et al.* VarDict: a novel and versatile variant caller for next-generation sequencing in cancer
010   research. *Nucleic Acids Res* **44**, e108 (2016).
011 70. DePristo, M.A.*, et al.* A framework for variation discovery and genotyping using next-generation
012   DNA sequencing data. *Nat Genet* **43**, 491-498 (2011).
013 71. McKenna, A.*, et al.* The Genome Analysis Toolkit: a MapReduce framework for analyzing next-
014   generation DNA sequencing data. *Genome Res* **20**, 1297-1303 (2010).
015 72. Kim, S.*, et al.* Strelka2: fast and accurate calling of germline and somatic variants. *Nature methods*
016   **15**, 591-594 (2018).
017 73. Cibulskis, K.*, et al.* Sensitive detection of somatic point mutations in impure and heterogeneous
018   cancer samples. *Nat Biotechnol* **31**, 213-219 (2013).
019 74. Li, H.*, et al.* The Sequence Alignment/Map format and SAMtools. *Bioinformatics* **25**, 2078-2079
020   (2009).
021 75. Cameron, D.L.*, et al.* GRIDSS: sensitive and specific genomic rearrangement detection using
022   positional de Bruijn graph assembly. *Genome Res* **27**, 2050-2060 (2017).
023 76. Feuerbach, L.*, et al.* TelomereHunter - in silico estimation of telomere content and composition
024   from cancer genomes. *BMC Bioinformatics* **20**, 272 (2019).
025 77. Blokzijl, F., Janssen, R., van Boxtel, R. & Cuppen, E. MutationalPatterns: comprehensive genome-
026   wide analysis of mutational processes. *Genome Med* **10**, 33 (2018).
027 78. Alexandrov, L.B.*, et al.* The repertoire of mutational signatures in human cancer. *Nature* **578**, 94-
028   101 (2020).
029 79. Mermel, C.H.*, et al.* GISTIC2.0 facilitates sensitive and confident localization of the targets of focal
030   somatic copy-number alteration in human cancers. *Genome Biol* **12**, R41 (2011).
031 80. Dobin, A.*, et al.* STAR: ultrafast universal RNA-seq aligner. *Bioinformatics* **29**, 15-21 (2013).
032 81. Robinson, M.D., McCarthy, D.J. & Smyth, G.K. edgeR: a Bioconductor package for differential
033   expression analysis of digital gene expression data. *Bioinformatics* **26**, 139-140 (2010).
034 82. Ritchie, M.E.*, et al.* limma powers differential expression analyses for RNA-sequencing and
035   microarray studies. *Nucleic Acids Res* **43**, e47 (2015).
036 83. Colaprico, A.*, et al.* TCGAbiolinks: an R/Bioconductor package for integrative analysis of TCGA data.
037   *Nucleic Acids Res* **44**, e71 (2016).
038 84. Kozomara, A., Birgaoanu, M. & Griffiths-Jones, S. miRBase: from microRNA sequences to function.
039   *Nucleic Acids Res* **47**, D155-D162 (2019).
040 85. Maksimovic, J., Gagnon-Bartsch, J.A., Speed, T.P. & Oshlack, A. Removing unwanted variation in a
041   differential methylation analysis of Illumina HumanMethylation450 array data. *Nucleic Acids Res* **43**,
042   e106 (2015).
043 86. Phipson, B., Maksimovic, J. & Oshlack, A. missMethyl: an R package for analyzing data from
044   Illumina's HumanMethylation450 platform. *Bioinformatics* **32**, 286-288 (2016).
045 87. Peters, T.J.*, et al.* Calling differentially methylated regions from whole genome bisulphite
046   sequencing with DMRcate. *Nucleic Acids Res* **49**, e109 (2021).

047   88.   Stuart, T., Srivastava, A., Madad, S., Lareau, C.A. & Satija, R. Single-cell chromatin state analysis with
048   Signac. *Nature methods* **18**, 1333-1341 (2021).
049   89.   Stuart, T.*, et al.* Comprehensive Integration of Single-Cell Data. *Cell* **177**, 1888-1902 e1821 (2019).
050   90.   Zhang, Y.*, et al.* Model-based analysis of ChIP-Seq (MACS). *Genome Biol* **9**, R137 (2008).
051   91.   Kurtenbach, S. & Harbour, J.W. SparK: A Publication-quality NGS Visualization Tool. *bioRxiv*, 845529
052   (2019).
053   92.   Fuchs, T.L.*, et al.* Expanding the clinicopathological spectrum of succinate dehydrogenase-deficient
054   renal cell carcinoma with a focus on variant morphologies: a study of 62 new tumors in 59 patients.
055   *Mod Pathol* **35**, 836-849 (2022).
056   93.   Fuchs, T.L.*, et al.* A Proposed Grading Scheme for Medullary Thyroid Carcinoma Based on
057   Proliferative Activity (Ki-67 and Mitotic Count) and Coagulative Necrosis. *Am J Surg Pathol* **44**, 1419-
058   1428 (2020).
059   94.   Henson, J.D.*, et al.* The C-Circle Assay for alternative-lengthening-of-telomeres activity. *Methods*
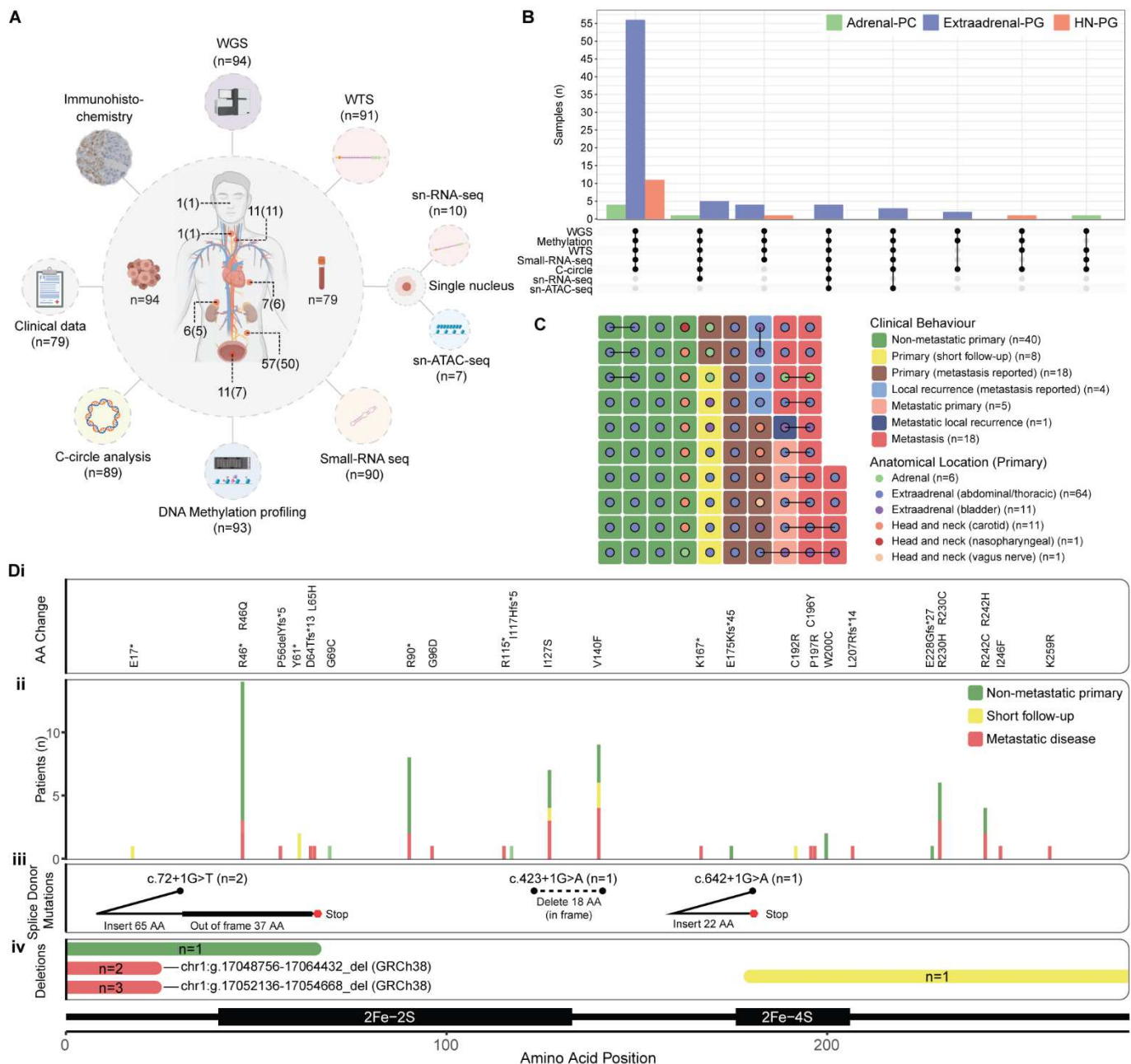060   **114**, 74-84 (2017).
061
062

Figure 1: Multi-omic analysis of SDHB-mutated PCPG

(A) *Outer ring:* Overview of the analytical methods applied to the cohort annotated with the number of tumours analysed. *Inner ring:* The number of tumours and patients (in parenthesis) analysed from each anatomical location. Where a metastasis was analysed, the location of the primary tumour is indicated. **(B)** A summary of the combination of analytical methods applied to each tumour with respect to anatomical primary location. The upper panel indicates the total number of samples from each anatomical location analysed with the respective combination of assays (lower panel). **(C)** Anatomical location (dot colour) and clinical behaviour (tile colour) of each tumour analysed. Paired samples from the same patient are joined by a line. **(D)** Summary of the germline *SDHB* mutations detected by WGS across the cohort and their respective position within the protein amino acid sequence. **(i)** Amino acid changes for single nucleotide variants and small insertion/deletion events (NP_002991.2). **(ii)** The total number of patients observed with each amino acid change where bar colour indicates the clinical disease course. **(iii)** Schematic of the consequence of splice donor mutations. **(iv)** Regions of the SDHB protein sequence deleted by large scale structural events. Bar colour indicates the clinical disease course and the number of patients affected is indicated within the bar.
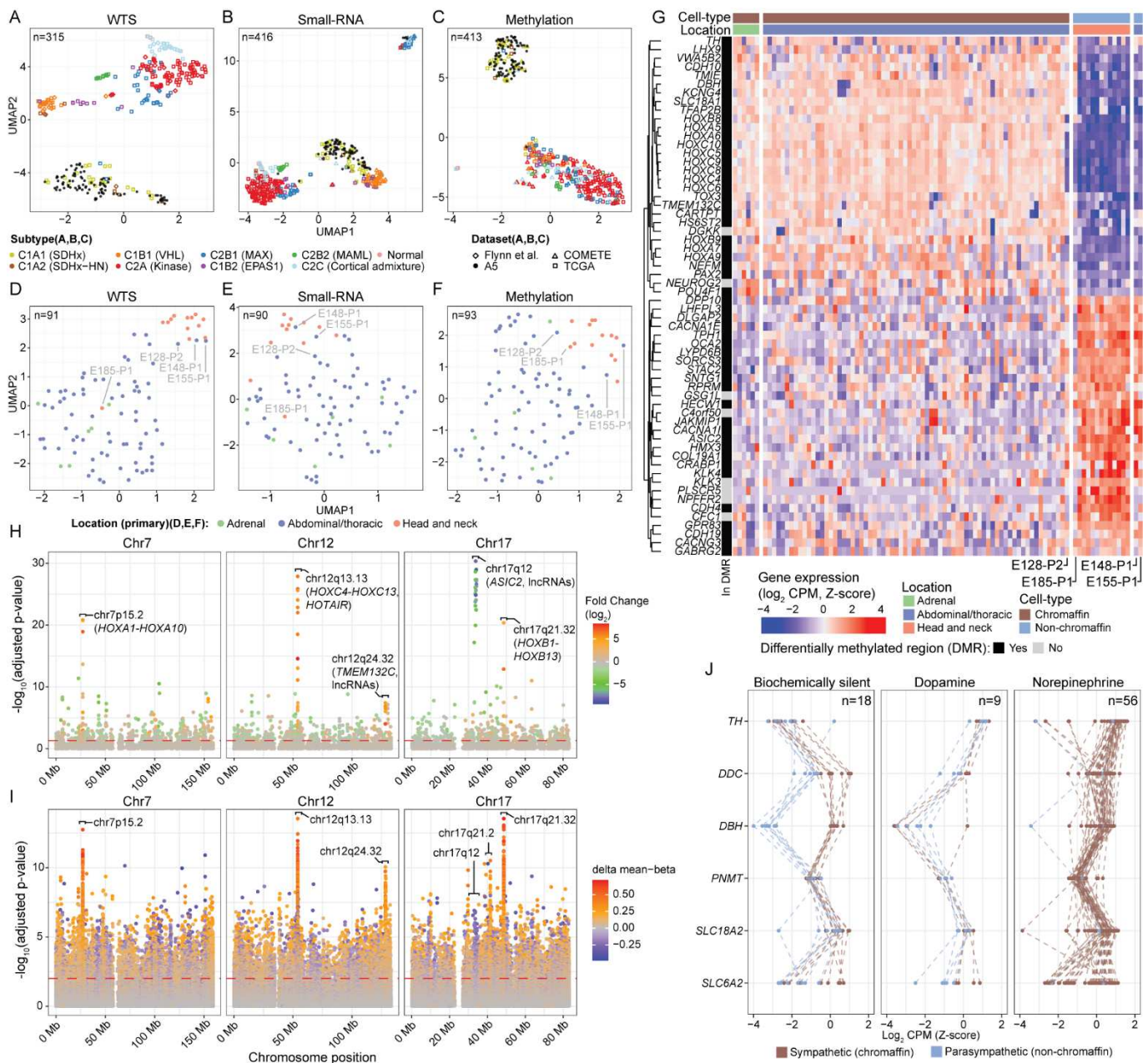
Figure 2: Genomic profiling separates sympathetic and parasympathetic PGL
UMAP dimensional reduction was used to cluster WTS (A), small-RNA-seq (B) and **DNA** methylation data (C) with previously published **data.** UMAP clustering was also repeated for respective A5 data types in isolation (D-F). **(G)** Differential expression profiling was performed between abdominal-thoracic PCPG and HN-PG. The heatmap shows CPM (log2, z-score) expression values for each tumour (x-axis) for the top differentially expressed genes (adjusted p-value < 0.05, ranked by log-fold-change, top and bottom 30 genes are shown)(y-axis). The top annotation bars indicate the suspected cell-of-origin based on UMAP clustering and the anatomical location of the tumour, respectively. The left annotation bar indicates whether the gene was also in a differentially methylated region for the same contrast. **(H/I)** Spatial distribution of adjusted p-values (y-axis, -log10) along chromosomes 7, 12, and 17 (x-axis) from differential expression **(H)** and probe-level differential methylation analysis **(I)** between sympathetic PCPG and HN-PG. **(J)** Expression of catecholamine biosynthesis and processing pathway genes. Line colour indicates the anatomical location of the tumour and sub-panels segregate tumours based on which catecholamines were above upper normal limit during clinical testing. Expression data for the A5 cohort were combined with a larger compendium of publicly available PCPG representing the different PCPG subtypes before values were normalized to Z-scores. Only A5 tumours are shown.
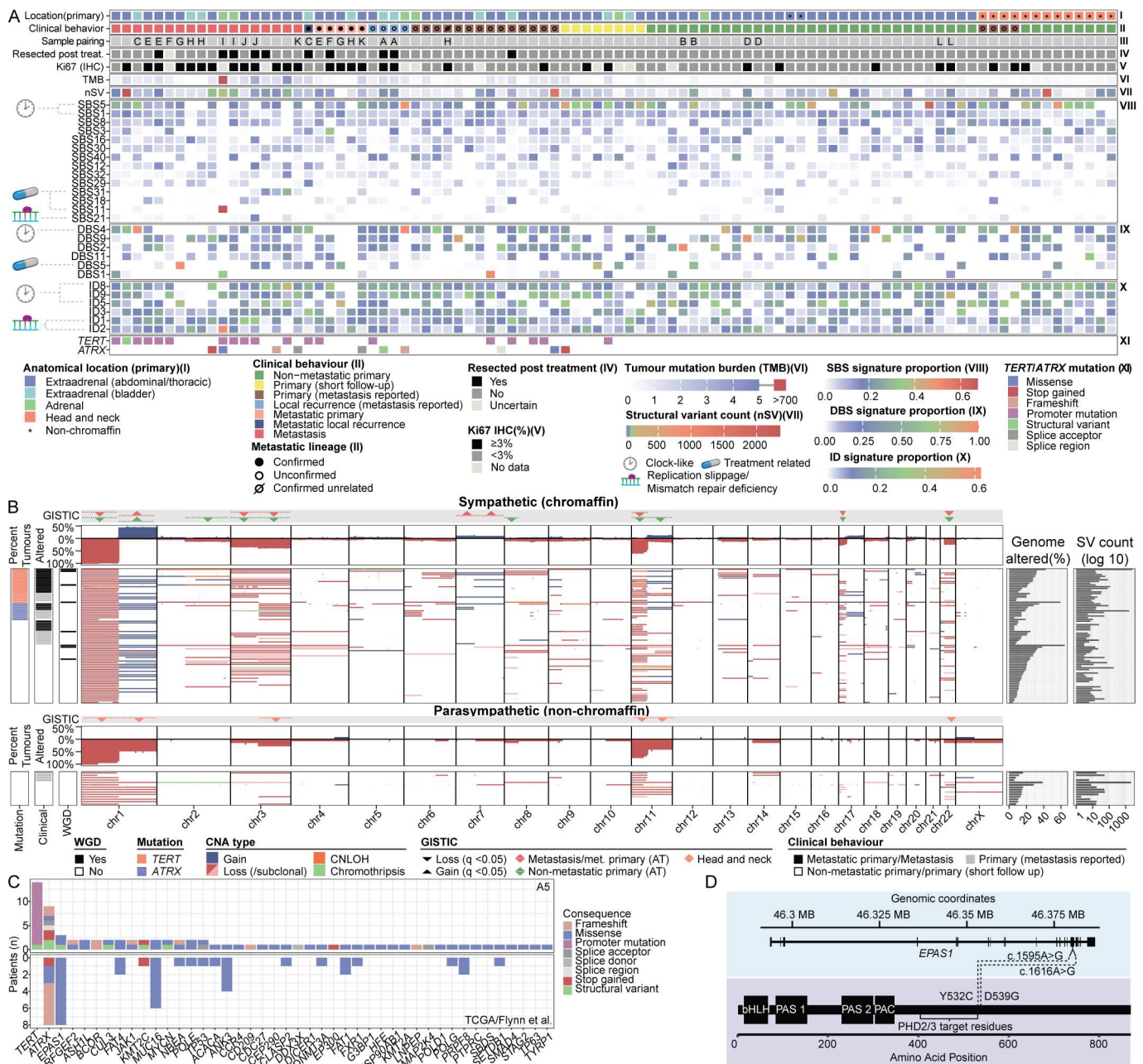
Figure 3: Genomic and clinical features of PCPG
(A)(i) Tile colour indicates the anatomical location of the tumour or, in the case of a metastasis, the associated primary tumour. An asterisk indicates whether the tumour had a non-chromaffin expression signature. **(ii)** Tile colour indicates the clinical behaviour of the tumour. Primary tumours resected from patients with metastatic disease are further annotated as to whether the tumour was able (filled circle) or unable (open circle) to be confirmed as the metastatic clone through sequencing of a paired metastasis. **(iii)** An identifier linking samples from the same patient. **(iv)** Indicates if the sample was resected after a cytotoxic treatment regime. **(v)** Immunohistochemical scoring of Ki67 expression, tumours with greater than 3% positive cells are indicated by a black square. **(vi)** Tumour mutation burden (mutations per megabase) and **(vii)** number of structural variants are indicated using a heatmap. **(viii-x)** Signature analysis was performed using the MutationalSignatures package for R. SBS signatures ranked (top to bottom) based on the mean proportional contribution of variants. Output was filtered to retain signatures that contributed 15% of mutations and at least 500, 50, or 10 mutations for SBS, ID, and DBS signatures, respectively, in at least one tumour. Colour indicates the proportion of mutations from each class attributable to the respective signature for a given sample. **(xi)** The presence of a TERT or ATRX mutation detected by WGS. **(B)** Aggregate and per-sample copy number aberrations detected by WGS in sympathetic (rows 2 and 3) and parasympathetic (rows 5 and 6) PCPG. Regions that were detected as significantly recurrently deleted (downward arrow) or amplified (upwards arrow) are indicated (rows 1 and 4). Clinical behaviour and the presence of whole genome doubling are annotated to the left of per-sample data (rows 3 and 5), while the percentage of genome altered and number of structural variants observed in each tumour are annotated on the right. Losses and gains as well as percent genome altered are expressed relative to sample ploidy rather than diploid. **(C)** Genes that were detected as recurrently altered by WGS and predicted to be drivers by Cancer Genome Interpreter across the A5 cohort (top) and the respective number of mutations observed in two previously published datasets (bottom). **(D)** Schematic showing the DNA and protein position of two somatic mutations observed in *EPAS1*.
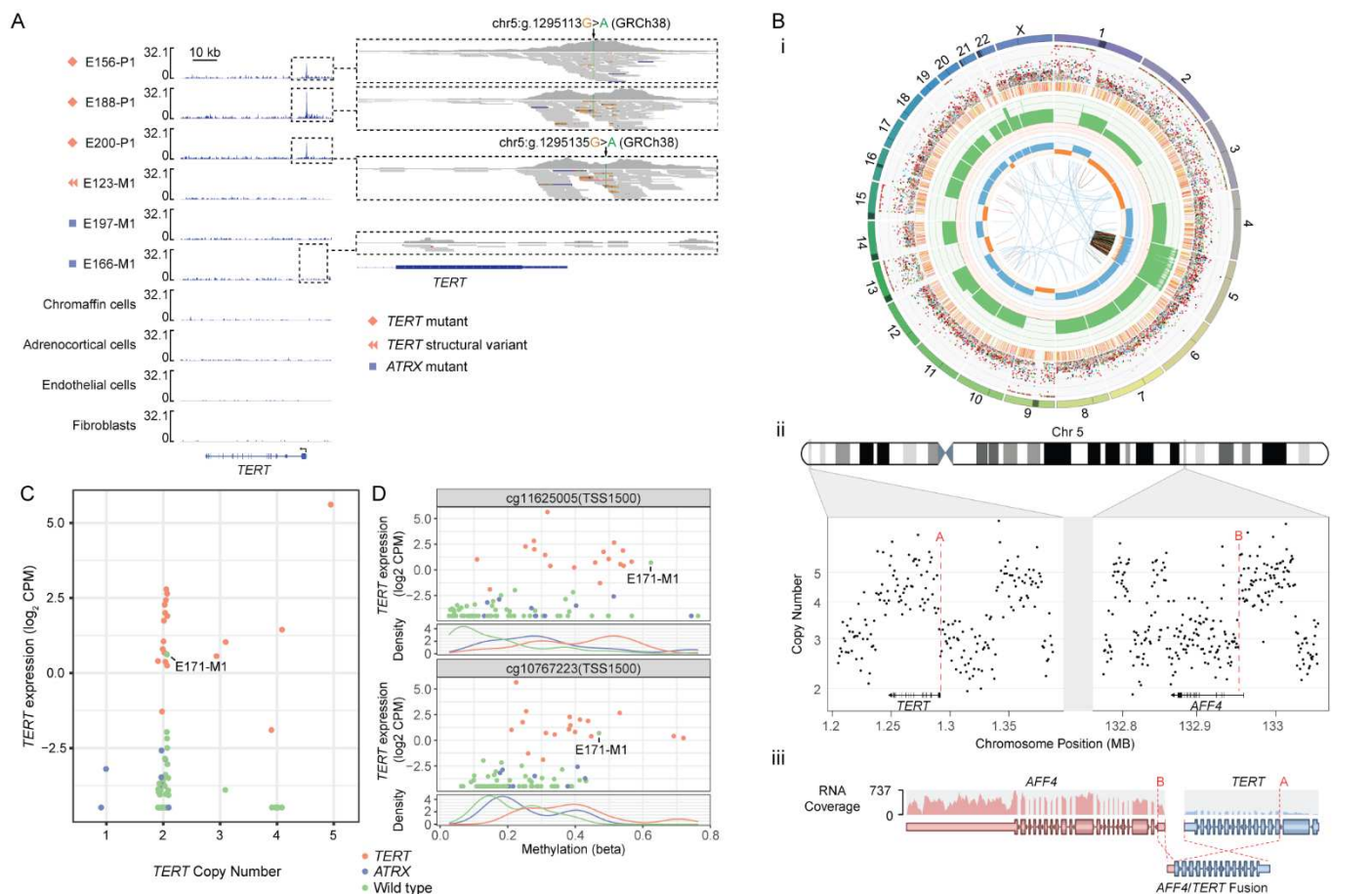
Figure 4. TERT promoter mutations and structural alterations
(A) sn-ATAC-seq covering the *TERT* gene and promoter (inset) region. Data is shown for tumour cells from two *ATRX* mutant tumours, three *TERT* mutant tumours, and one tumour with a TERT structural variant. Normal chromaffin, adrenocortical, fibroblast, and endothelial cells are shown for contrast. (B)(i) Circos plot describing somatic alterations detected by WGS in E123-M1. Outer ring indicates chromosome, second outer ring marks SNVs (blue: C>A, black: C>G, red: C>T, grey: T>A, green: T>C, pink: T>G) and Indels (yellow: insertions, red: deletions). Third outer ring indicates total copy number, (green: >2, red: <2), the fourth outer ring indicates the copy number of the minor allele (blue: >1, orange: <1). The center circle displays structural variants. **(ii)** Copy number segmentation data from the *AFF4* and *TERT* gene regions in E123-M1 showing multiple short segmental copy-number changes due to chromothripsis. The break points contributing to an *AFF4-TERT* fusion are marked with red dashed lines. **(iii)** Schematic of *AFF4-TERT* fusion detected by WTS. **(C)** *TERT* expression (y-axis, log2 CPM) versus gene copy number at the TERT locus (x-axis) **(D)** *TERT* expression (y-axis, log2 CPM) versus the methylation status (x-axis) of probes in the *TERT* promoter and *TERT* hypermethylated oncological regions (rows 1 and 3). Density plot of probe methylation beta-values (rows 2 and 4). Point and line colour indicate *TERT*/*ATRX* mutation status.
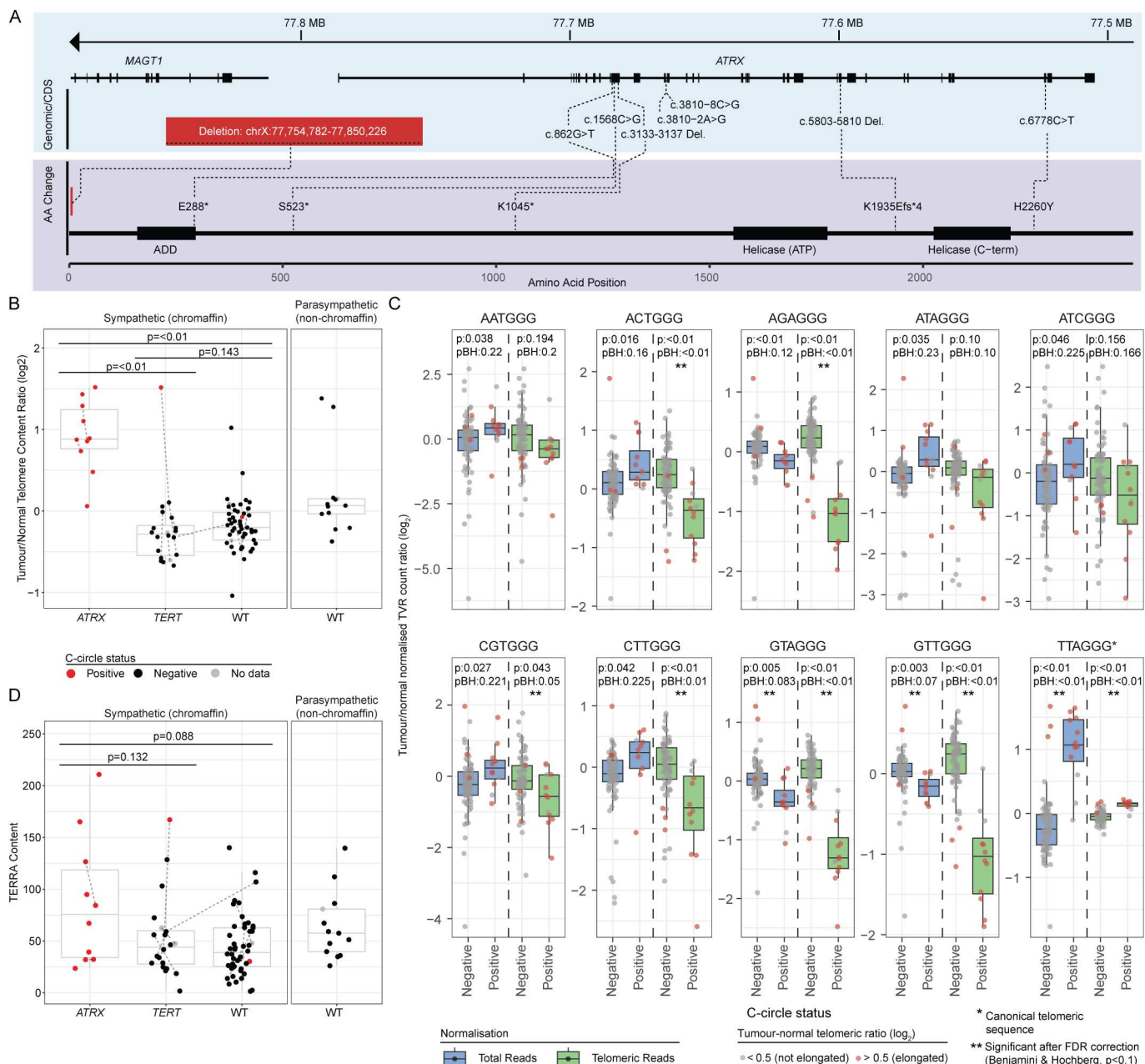
Figure 5: Loss of *ATRX* leads to telomere dysregulation

(A) Genomic (top) and protein (bottom) position of alterations detected in the *ATRX* gene by WGS. **(B)** Ratio of tumour to normal telomere read content (y-axis) in relation to *ATRX* and *TERT* mutation status (x-axis). Presence (red) or absence (black) of C-circles is indicated by the dot colour. Paired tumours from the same patient are joined by a dashed line. A two-sided Student's t-test was used to test for differences. Values were averaged across paired tumours prior to statistical testing. **(C)** Telomere variant repeats (TVRs) of the type NNNGGG (and the reverse complement) were detected in WGS data from tumour and matched normal using TelomereHunter. Count values were normalized against intratelomeric read count (green) or total read count (blue). The tumour/normal ratio of normalized counts (y-axis) are shown with respect to the presence or absence of detected c-circles (x-axis). Only TVR sequences that were significantly different using a Students t-test (p<0.05) applied to values normalized to total reads are shown. TVRs that were significant after false-discovery correction (Benjamini & Hochberg, p<0.1) are indicated with a double-asterisk. P-values before (p) and after (pBH) correction are shown. Data points are coloured to indicate a tumour/normal telomere content ratio (log2) greater than (red) or less than (grey) 0.5 **(D)** Reads containing telomeric sequences were counted from WTS data using TelomereHunter. The telomeric content (y-axis) was computed as the number of unmapped reads containing telomeric sequence times 1,000,000 divided by the total number of reads with a GC content similar to telomeric repeats. Data point colours, x-axis, and statistical testing are as described in panel B. The lower and upper hinges of each boxplot correspond to the first and third quartiles, respectively, and the median value is marked. The whiskers extend to the largest and smallest value no greater than 1.5 times the interquartile range above or below the upper and lower hinges, respectively.
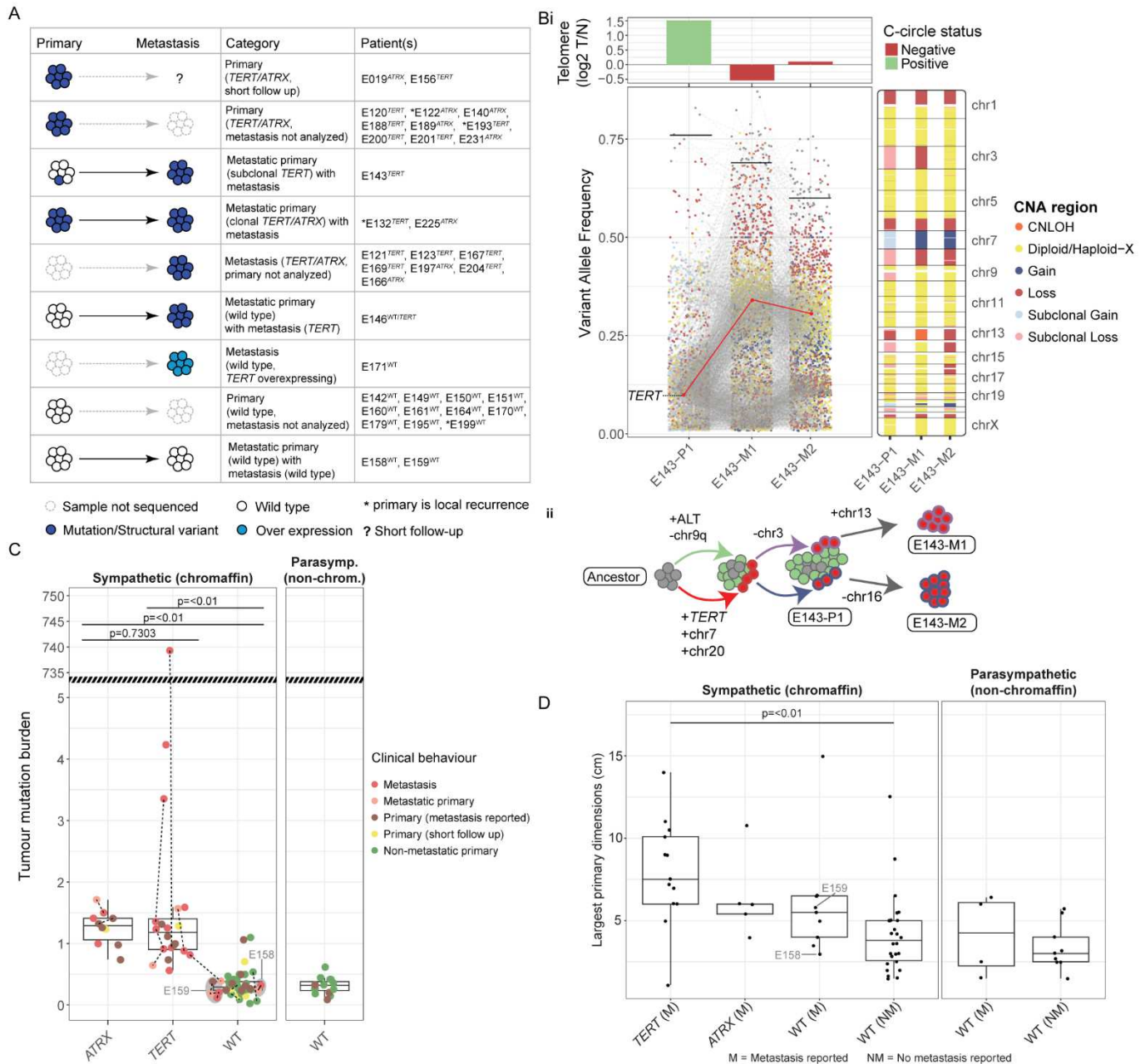
Figure 6: *TERT*/*ATRX*-alterations and their association with metastatic progression

(A) A schematic illustrating the case categories with presence or absence of *TERT*/*ATRX* mutations in primary and paired metastatic tumours. **(B)** A polyclonal primary harbouring ALT and p*TERT* mutations giving rise to metastases **(i)** The centre panel shows the variant allele frequency (VAF, y-axis) for all somatic mutations detected in a metastatic primary (E143-P1) and the two paired metastases (E143-M1/2) from patient E143 (x-axis). The colour of each dot denotes the genomic copy number status in the region of each variant. The horizontal lines indicate the purity of each tumour and can be read as a proportion from the x-axis. Grey lines connect mutations shared across the paired tumours while a p*TERT* mutation is highlighted with a red line. The top panel shows the tumour to normal telomere content ratio for each tumour and the colour of each bar indicates the presence or absence of C-circles. The panel on the right shows the genomic copy number status along each chromosome (y-axis) for each tumour (x-axis). **(ii)** A schematic illustration of the clonal evolution of metastatic disease in patient E143. The cell colour indicates the presence of the ALT phenotype (green) or p*TERT* mutation (red). **(C)** The tumour mutation burden (mutations per megabase, y-axis) observed in each tumour with respect to *TERT*/*ATRX* gene mutation status (x-axis). A one-tailed Student's t-test was used. The y-axis has been truncated to accommodate an extreme outlier which was excluded during statistical testing. (D) The dimensions (centimetres, y-axis) of the largest primary tumour reported for each patient. Patients are stratified by the presence of a *TERT*/*ATRX* mutation and the presence (M) or absence (NM) of metastatic disease. The lower and upper hinges of each boxplot correspond to the first and third quartiles, respectively, and the median value is marked. The whiskers extend to the largest and smallest value no greater than 1.5 times the interquartile range above or below the upper and lower hinges, respectively. A one-tailed Student's t-test used to test for significance.
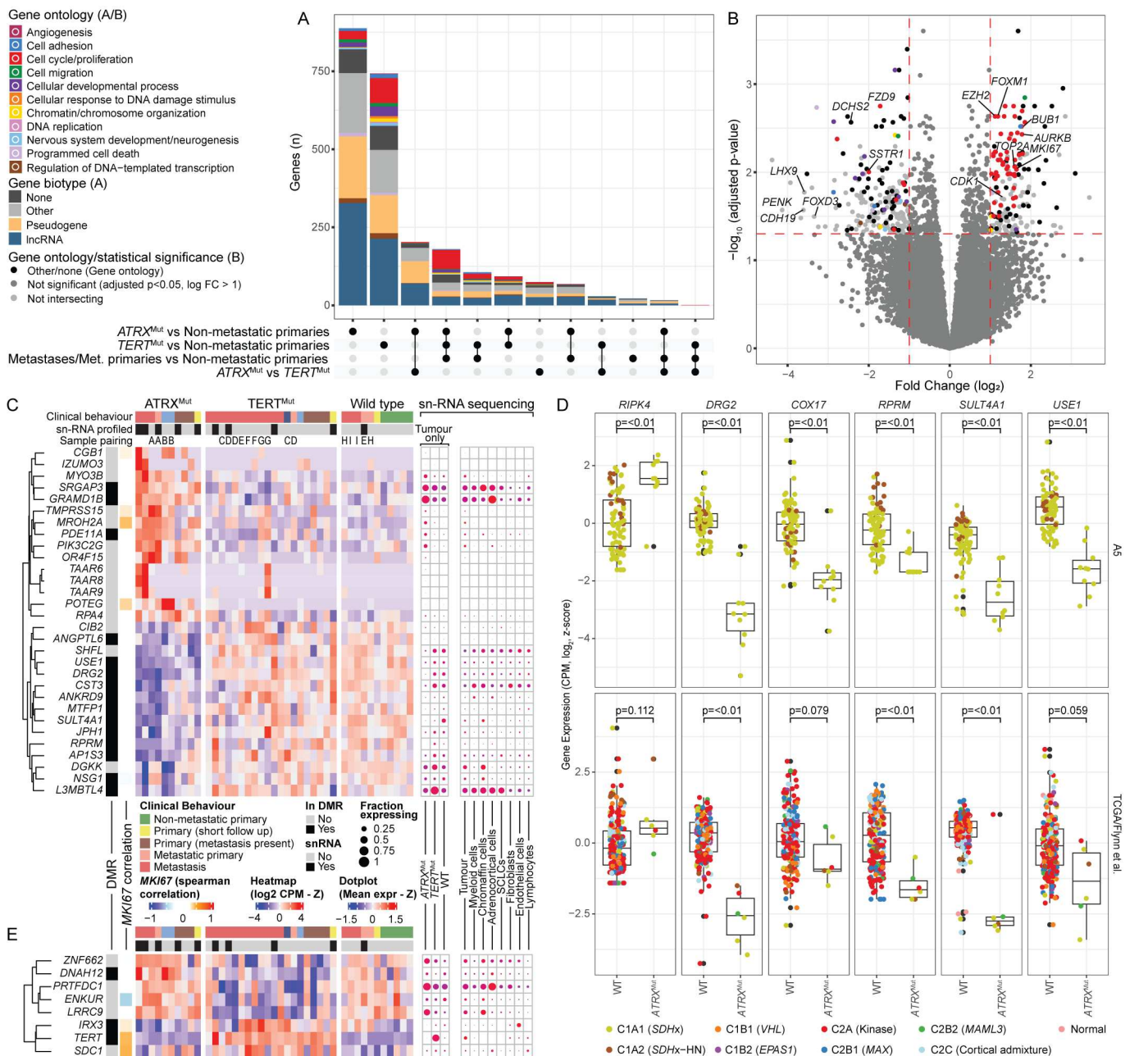
Figure 7: Differential gene expression between *TERT* and *ATRX*-altered and non-metastatic tumours

Differential gene expression analysis was performed contrasting non-metastatic primary tumours with either (i) *ATRX* mutant tumours, (ii) *TERT* mutant tumours, or (iii) all metastasis and confirmed metastatic primaries. A fourth contrast between *TERT* and *ATRX* mutant tumours was also performed. **(A)** An upset plot showing the intersection of genes that were significant (adjusted p-value < 0.05, log-fold-change > 1) in each contrast. Bar colour indicates gene-ontology association for protein coding genes or gene biotype for non-protein-coding genes. **(B)** Differential gene-expression between non-metastatic primary and metastatic tumours showing fold change (log2, y-axis) versus adjusted p-value (-log10, x-axis). Genes that were also significant in non-metastatic primary vs TERT-altered and non-metastatic primary versus *ATRX*-altered contrasts are coloured according to gene ontology annotation. **(C)** Heatmap (centre panel) showing genes that were differentially expressed in both the *ATRX* vs non-metastatic primary and *ATRX* vs *TERT* contrasts. Annotation bars on the left indicate whether the gene was also found in a differentially methylated region (*ATRX* vs non-metastatic primary), and the correlation of the expression of *MKI67* to the expression of each gene (Spearman correlation). The right panel shows the gene expression determined by snRNA-seq in cells aggregated by cell type (right sub-panel) or *ATRX*/*TERT* mutation status (left sub-panel). Dot colour indicates mean expression while dot size indicates the fraction of cells expressing the gene. **(D)** Expression (log2 CPM, y-axis) of genes found to be differentially expressed between *ATRX*-altered and non-metastatic primary tumours. Expression data is shown from the A5 cohort (top) and the TCGA/Flynn et al. cohorts (bottom). Data point colour indicates PCPG subtype. A Student's t-test was used to test for differences **(E)** Differentially expressed genes in both the *TERT*-altered vs non-metastatic primary and *ATRX*-altered vs *TERT*-altered contrasts. See panel C description for panel elements. The lower and upper hinges of each boxplot correspond to the first and third quartiles, respectively, and the median value is marked. The whiskers extend to the largest and smallest value no greater than 1.5 times the interquartile range above or below the upper and lower hinges, respectively.
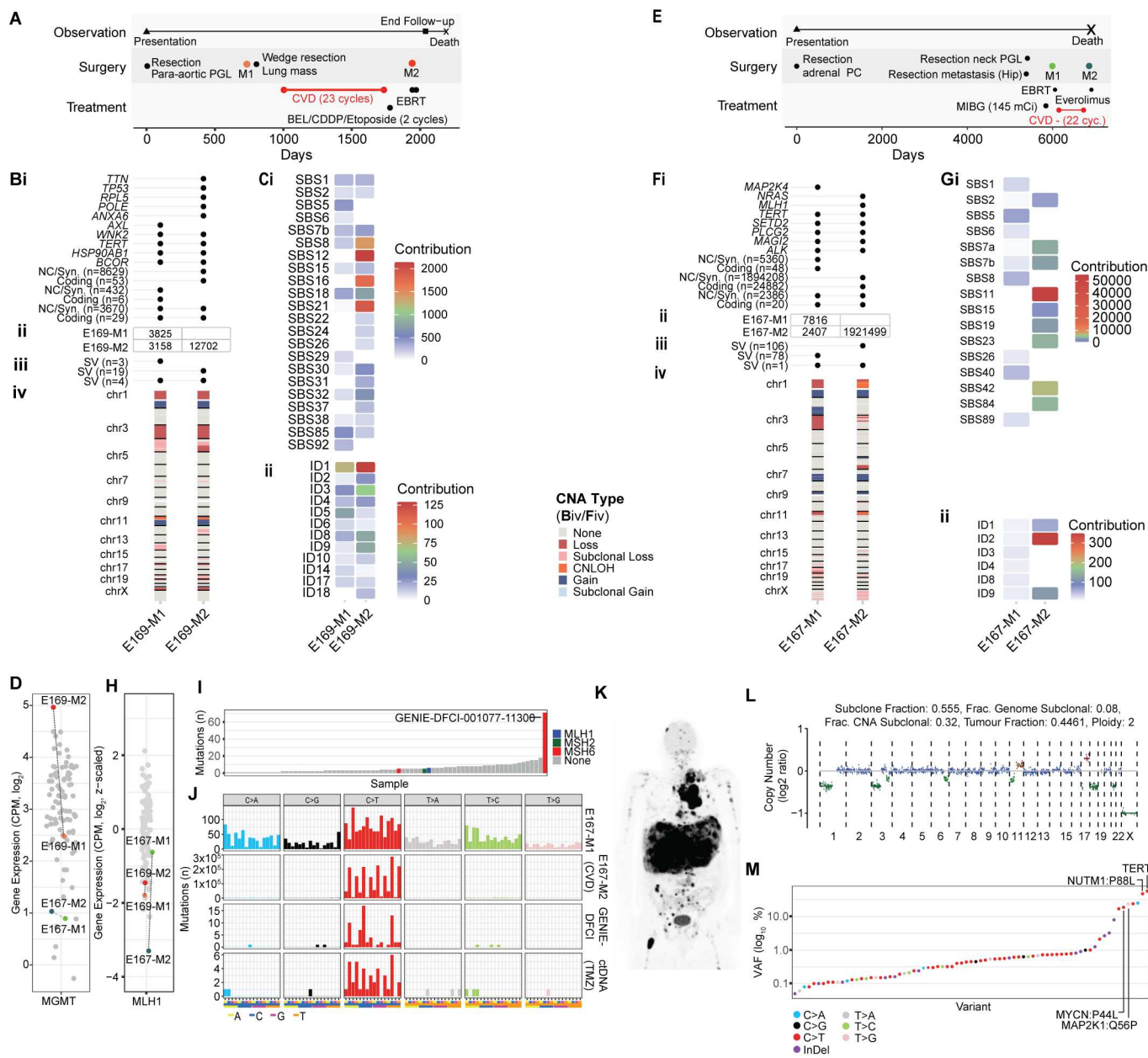
192
193 **Figure 8: Evolution of PCPG under treatment pressure**
194 **(A)** Clinical timeline of for patient E169. **(Bi)** Shared and private variants (y-axis) between paired metastases (x-axis) taken before
195 and after CVD treatment. **(Bii)** Total number of variants detected by WGS (top left, bottom right) and number of variants shared
196 between tumours (bottom left). **(Biii)** Shared and private structural variants between paired metastases. **(Biv)** Copy number status
197 along each chromosome (y-axis) in paired metastases (x-axis). **(C)** Mutation signature analysis using COSMIC v3 SBS **(i)** and
198 InDel **(ii)** signatures (y-axis) in paired metastases (x-axis). Heatmap colour indicates signature contribution. **(D)** Expression of
199 *MGMT* in the A5 cohort. **(E-G)** Patient E167, see description for panels B-C. **(H)** Expression of *MLH1* in the A5 cohort. **(I)** Total
200 mutation counts (y-axis) for PCPG tumours (x-axis) in the Project GENIE data registry. Bar colour indicates the presence of a
201 mutation in the mismatch repair pathway. **(J)** Trinucleotide context for mutations observed in E167-M1 (top), E167-M2 (second
202 from top), the highest mutation load tumour from the GENIE dataset (second from bottom), and ctDNA derived from a patient
203 with metastatic SHDB-related PGL treated with Temozolomide. **(K)** ^{18}F-FDG-PET imaging for Temozolomide treated patient at
204 time of blood draw for cfDNA analysis. **(L)** Ichor CNA analysis of ctDNA derived from Temozolomide treated patient **(M)**
205 Variant allele frequencies (y-axis) for somatic variants (x-axis) observed in ctDNA derived from Temozolomide treated patient.
206 Datapoints are coloured to indicate transition/transversion or insertion/deletion type.

Supplementary Files

This is a list of supplementary files associated with this preprint. Click to download.

- nreditorialpolicychecklistFlynn.pdf
- supplementaryfigures.pdf
- Supplementarydata1.xlsx
- Supplementarydata2.xlsx
- Supplementarydata3.xlsx
- Supplementarydata4.xlsx
- Supplementarydata5.xlsx
- Supplementarydata6.xlsx
- Supplementarytable1.pdf
- Supplementarytable2.pdf